Formation of carbon nanotubes: *In situ* optical analysis using laser-induced incandescence and laser-induced fluorescence

M. Cau,[1] N. Dorval,[1,*] B. Attal-Trétout,[1] J.-L. Cochon,[1] A. Foutel-Richard,[1] A. Loiseau,[2] V. Krüger,[3] M. Tsurikov,[3] and C. D. Scott[4,†]

[1]*ONERA, Chemin de la Hunière, 91761 Palaiseau Cedex, France*

[2]*Laboratoire d'Etude des Microstructures, ONERA-CNRS, BP 72, 92322 Châtillon Cedex, France*

[3]*Institut für Verbrennungstechnik, DLR, Pfaffenwaldring 38-40, D70569 Stuttgart, Germany*

[4]*Lyndon B. Johnson Space Center ES4, NASA, Houston, Texas 77058, USA*

(Received 19 November 2009; published 8 April 2010)

Gas-phase production of carbon nanotubes in presence of a metal catalyst with a continuous wave CO_2 laser is investigated by combining coherent anti-Stokes Raman scattering (CARS), laser-induced fluorescence (LIF), and laser-induced incandescence (LII). These *in situ* techniques provide a unique investigation of the different transformation processes of the primarily carbon and metal vapors issued from the vaporization of the target by the laser and the temperature at which these processes occur. Continuous-wave laser provides with stable continuous vaporization conditions very well suited for such *in situ* investigations. Temperature profiles inside the reactor are known from CARS measurements and flow calculations. Carbon soot, density, and size of carbon aggregates are determined by LII measurements. LIF measurements are used to study the gas phases, namely, C_2 and C_3 radicals which are the very first steps of carbon recombination, and metal catalysts gas phase. Spectral investigations allow us to discriminate the signal from each species by selecting the correct pair of excitation/detection wavelengths. Spatial distributions of the different species are measured as a function of target composition and temperature. The comparison of LIF and LII signals allow us to correlate the spatial evolution of gas and soot in the scope of the different steps of the nanotube growth already proposed in the literature and to identify the impact of the chemical nature of the catalyst on carbon condensation and nanotube nucleation. Our study presents the first direct evidence of the nanotube onset and that the nucleation proceeds from a dissolution-segregation process from metal particles as assumed in the well-known vapor-liquid-solid model. Comparison of different catalysts reveals that this process is strongly favored when Ni is present.

DOI: 10.1103/PhysRevB.81.165416 PACS number(s): 81.07.De, 81.16.Mk

I. INTRODUCTION

Various methods have been developed for the production of single-wall carbon nanotubes (SWCNTs) which are based on carbon vaporization at high temperature.[1–6] Laser vaporization belongs to these techniques together with arc discharge[1] and solar-energy furnace processes.[5] The carbon and catalysts evaporate simultaneously in the temperature range 3000–5000 K; but nanotubes are formed at lower temperatures, probably around 1400–1600 K.

A general phenomenological model (vapor-liquid-solid) was drawn up by Gavillet *et al.*,[7–9] based on careful high-resolution transmission electron microscopy (TEM) observations of samples produced by different techniques (arc discharge, laser vaporization, catalytic methods). The model is an extension of a model from Saito *et al.*,[10] describing nanotube growth from large catalytic particles. The formation of the SWCNTs proceeds first through the dissolution of carbon atoms into liquid metal particles [step (a)]. Beyond a saturation threshold, carbon precipitates at the surface of the particle [step (b)] in the form of tubes. The growth [step (c)] requires further incorporation of carbon feedstock at the nanotube-particle interface. The model is fully supported by quantum-molecular-dynamics simulations.[7,11,12]

However, there are still unresolved questions, especially concerning steps (a) and (b). What is the exact role of metal catalysts? How does its chemical composition influence the nucleation? What is the role of the temperature and concentration gradients in the gas and liquid phases? How do they affect the sequence of events?

In order to study these phenomena, we have applied laser-based diagnostic techniques to perform *in situ* diagnostics of the gas phase and of the carbon soot in a dedicated synthesis reactor. This reactor is based on the vaporization of a target by a continuous-wave (cw) CO_2 laser at constant surface temperature and vacuum pressure in a continuous flow of inert gas so that SWCNTs are produced in stable conditions.[13] Since the gas flow rate around the target is rather slow (50 ml s^{-1}), heat transfer and diffusion are the dominant transport phenomena in the fluid dynamics modeling of the continuous synthesis process.[14] The nature, the quality, and the quantity of the products have been probed.[15]

Optical diagnostics have already been applied to SWCNTs formation using pulsed laser ablation techniques.[2–4,16,17] A continuous vaporization reactor has noticeable advantages for performing *in situ* diagnostics: (i) the target evaporation is assumed to be nearly constant over the run duration and (i) measurements are made over a long period of time, (ii) reproducibility is readily monitored, (iii) transient evolution of the gas concentration resulting from pulsed ablation processes can be ignored, and (iv) successive steps of nanotube formation can be merely related to the spatial location above the target and to the temperature gradient along the vertical gas flow axis.[14,18]

In this study, laser-induced fluorescence (LIF) and laser-induced incandescence (LII) techniques have been used to

investigate the chemical species present in the gas phase and the carbon soot as a function of the distance from the vaporized target surface. LIF has been shown to be an appropriate technique for probing C_2 and C_3 radicals and metal gas phases.[2–4,16,17] Previous spectral investigations have allowed us to select pertinent pairs of excitation/detection wavelengths for each species.[18] The signals are measured as a function of height (h) above the target, yielding the vertical evolution of relative concentrations. Spatial investigations of the fluorescence signals in the hot carbonaceous flow are performed as a function of target composition and target temperature (T_s) up to 3500 K. The LII technique has been applied, to the analysis of the spatial distribution of the carbon soot and has been shown to provide a quantitative measurement of the primary size of carbon particles, thanks to a model developed at DLR.[19]

Both LIF and LII measurements have been correlated with previous temperature measurements performed by coherent anti-Stokes Raman scattering (CARS).[14,18] Furthermore, using appropriate velocity and temperature profiles, species concentrations have been calculated from a specific fullerene/soot/metal clusters model of the reacting gas flow developed by Scott[20] and compared with our measurements.[21]

Since nature of the catalyst can critically influence the SWCNTs formation and yield, various combinations of catalysts have been tested in order to quantitatively relate the concentration and the nature of the gas species with the soot behavior. The results show how both carbon and metal condense from their initial gaseous state and how the metal condensation influences that of carbon. Combination of CARS, LIF and LII is shown to provide a direct evidence of the nanotube onset in the reactor.

The paper is organized as follows. The continuous laser vaporization reactor, its operating conditions and temperature characteristics are first described (Sec. II). Section III presents LIF measurements and Sec. IV outlines the results of *ex situ* analysis of metal nanoparticles by transmission electron microscopy. Section V describes LII measurements and Sec. VI deals with the behavior of iron by cross-correlating LIF and LII results. In Sec. VII, all measurements are cross correlated and discussed. Main results are finally summarized in Sec. VIII.

II. cw LASER VAPORIZATION

The reactor is presented in Ref. 18. It is equipped with three fused silica windows for laser diagnostics. A 5-mm-diameter target rotating at 280 r min^{-1}, is located at the center of the reactor. Helium is injected at the bottom of the cylindrical chamber, and flows around the target at a rate of 50 ml s^{-1} and a pressure of 300 hPa. An upper silica tube, 20 mm in diameter, used for gas outflow and nanotube collection, is placed 22 mm above the target.[14] The cw CO_2 laser irradiates the target at 45° incidence angle from the top of the reactor. The whole surface is irradiated, thanks to the cone geometry achieved by focusing the beam about 15 mm below the target surface (Fig. 1). Various target compositions have been used for the laser-based diagnostics of the vaporized plume: pure carbon, C:Co (98:2 at. %), C:Co:Y (94.8:4.2:1 at. %), C:Ni (98:2 at. %), C:Fe (98:2 at. %), and C:Co:Ni (96:2:2 at. %). The targets are homemade starting with graphite powder (Goodfellow, purity 99.8%) pressed with weighted amount of metal powders (Goodfellow, purity 99.8%). They contain also iron and calcium impurities as revealed by the analysis of the spectral content of emission spectra.[18,22] A chemical analysis using spark emission spectroscopy of the homemade target was also performed and provides with the metallic impurities amount. The iron behavior is discussed in details in Sec. VI.

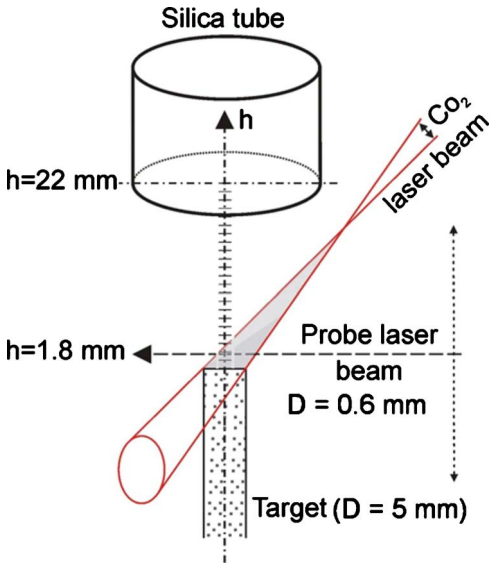

FIG. 1. (Color online) Region of *in situ* optical measurements.

The laser power can be varied up to 1500 W. The surface temperature of the target, T_s, is measured with an optical pyrometer. This temperature is maintained at a constant value by regulating the laser power in order to achieve stable and reproducible vaporization. The target is translated upwards during the run to compensate for material loss and keep its active surface fixed in space. We take care to prepare homogeneous and well-compacted targets to promote a laminar flow of soots in regular vaporization conditions. A run sequence is shown in Fig. 2(a). It displays the CO_2-laser power vs time during the run. The target surface temperature given by the pyrometer and the C_2 fluorescence signal measured at 0.5 mm above the target are also shown. That typical run involves three periods of time: (i) the starting phase of 20 s in duration, (ii) a stable phase, and (iii) a phase of unstable laser power and target temperature. This time sequence is representative of the various regimes of vaporization occurring during a run: (i) a transient regime resulting from the irradiation of the CO_2-laser beam on the cold target, which causes a sudden rise of the surface temperature and the expellation of metal-carbon particles from the target surface, (ii) a stationary regime of vaporization which is established when conduction and convection reach steady-state conditions, and (iii) an unstable regime due to the formation of protuberances on the target that disturbs the flow by distorting target illumination. The vaporization rate (V_v) is

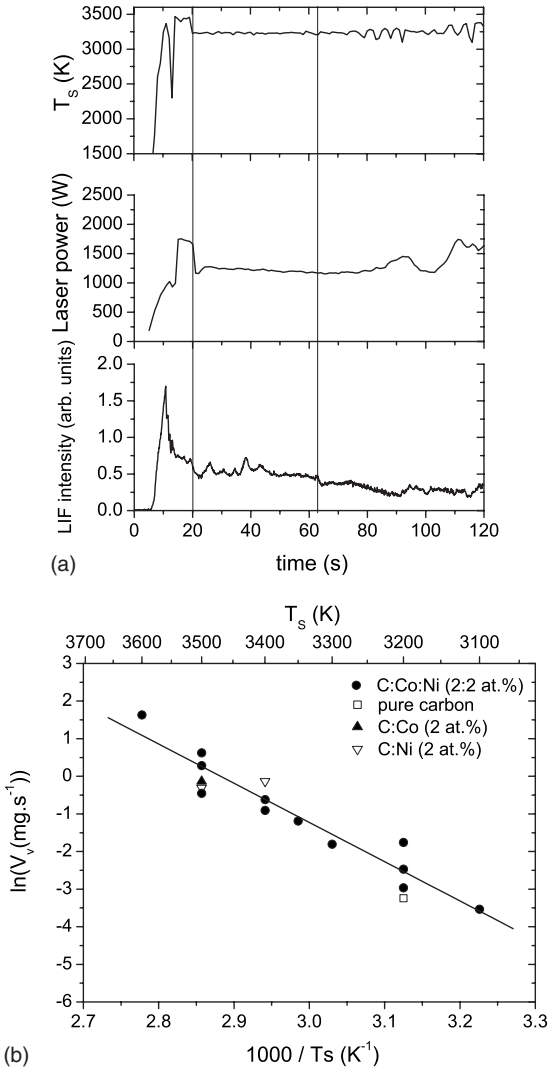

FIG. 2. (a) Simultaneous recording of the run conditions vs time: (top) the surface temperature of the target (T_s), (middle) CO_2-laser power, (bottom) intensity of LIF signal of C_2 measured at an height of 0.5 mm. (b) Vaporization rate (V_v) vs inverse T_s for various target compositions.

100 μg s^{-1} at T_s=3300 K and increases up to 1 mg s^{-1} at T_s=3500 K, for all target compositions [Fig. 2(b)]. A weighting procedure is used to measure the vaporization rate of different type of targets.[14,22] An Arrhenius plot is drawn from the solid carbon evolution. It will be compared later to that of gaseous carbon (Sec. III A).

When the target temperature, gas pressure, and helium flow rate are, respectively, 3500 K, 300 hPa, and 50 ml s^{-1}, SWCNTs of high quality and purity are produced.[9,12,14,15] Vaporization of the graphite target occurs at a surface temperature which lies below the temperature of the graphite sublimation (near 4000 K). The vaporization regime is driven by diffusion through the formation of a mass transfer layer as explained by Laplaze *et al.*,[5] who used the solar-energy furnace of the Odeillo Institute to produce carbon nanotubes.

In this vaporization layer, carbon vapor is in thermodynamic equilibrium with the surface; the partial pressure at the surface is equal to the vapor pressure at equilibrium. Accordingly, even for surface temperature (T_s=3000–3500 K) lower than the sublimation point, carbon vaporization may occur. In this layer, which is about 1 mm thick as determined from previous emission spectra,[18,22] carbon dilution by diffusion of helium onto the surface has been estimated from a separate study at T_s=3500 K.[20] All the carbon and metallic species which are evaporated within this vaporization layer are cooled and diluted by mixing with the annular helium flow. The vaporization layer appears as a bright after glow due to light emission originating from heated and excited atoms and molecules.[18,22] At about 1 mm above the surface and 20 s after the CO_2-laser power is switched on, laser vaporization reaches the steady state regime [Fig. 2(a)] during which the gas phase evolution can be inspected and effective *in situ* measurements started. They consist in probing using LIF and LII techniques the evolution of the gaseous species (populations and concentrations) and of the soot particles in order to characterize the hot synthesis process. Measurements are stopped when flow instabilities are seen or irregular protuberances are formed on the target surface, which preclude clear detection of optical signals.

Previous CARS measurements have shown that the shape of the temperature profile does not depend on the target temperature. The temperature profile was calculated at T_s =3500 K using the MSD code developed at ONERA.[14] The calculated and measured CARS temperature profiles are displayed in Fig. 3; three separate thermal regions have been previously defined in the hot flow[18] as shown in Fig. 3(b). In the first region, fast cooling takes place over about 3.5 mm, down to a gas temperature of about 2100 K. In the second region, the cooling is slower as indicated by the change in the slope between 3.5 and 7.5 mm. This region ends with a temperature of 1600 K, near the eutectic temperature of Ni-C (1599 K) and Co-C (1593 K), but above the eutectic temperature of Fe-C (at most 1525 K for Fe_3C) and below the Y-C temperature (at most 2563 K for YC_2), as given in Table I. It is worth noting that the melting temperature of Ni-C, Co-C, and Fe-C alloys is more than 128 K lower than the melting point of the pure metal. On the other hand, YC_2 carbide has a melting temperature far higher than that of pure yttrium, i.e., 2563 K compared to 1795 K (see Table I).

In the third region, from 7.5 mm to the entrance of the collection tube, the temperature is nearly flat, around 1000 K [Fig. 3(b)]. It seems reasonable to describe the thermal evolution of the plume as a sequence of a high cooling rate (region 1) followed by a long residence time in the range of 2100–1000 K (regions 2–3).[14,18,22] The definition of the different temperature regions may appear as arbitrary at this step. The separation in three regions will be justified later; it relies on the first observation of Foutel[14] and is confirmed by the present LIF and LII diagnostics.

III. LIF ANALYSIS OF GAS COMPOSITION

The LIF setup was presented in a previous paper.[18] A pulsed Nd:YAG (yttrium aluminum garnet) laser (355 nm) with a 10 Hz repetition rate is used to pump a dye laser (Quantel, TDL 90). The dye laser, operating with Coumarin

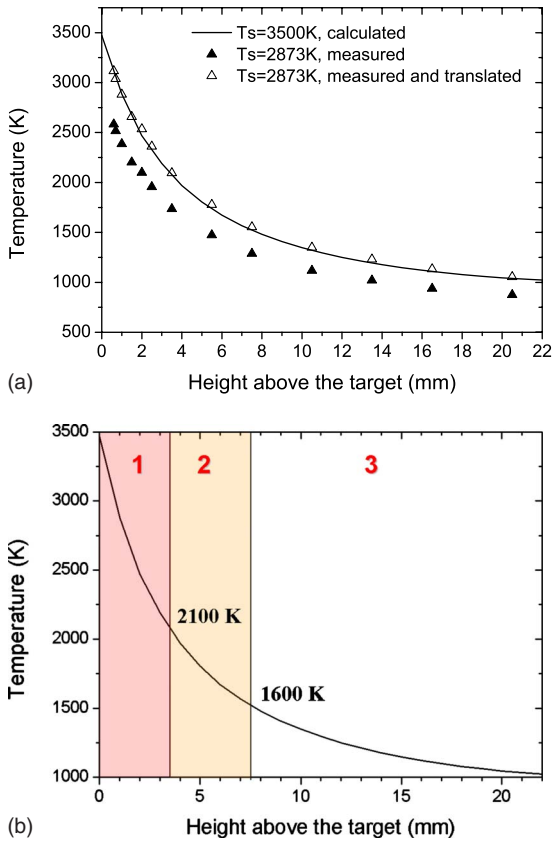

FIG. 3. (Color online) (a) Calculated temperature profile in He (300 hPa, 50 ml s^{-1}) at T_s=3500 K(solid line). Measured CARS temperature profile for a C:Co:Ni (2:2 at. %) in He/H_2 (10 vol %) at T_s=2873 K (filled triangles) and its translation homothetic by a factor of 1.22 (open triangles). (b) Three thermal regions are defined.

440, directly excites C_2 and C_3 radicals at 438 nm and 432 nm, respectively. The laser emission of Coumarin 500 dye is frequency doubled in a BBO crystal near 248 nm for metal atom excitation. The laser linewidth is about 0.08 cm^{-1} in the visible and 0.12 cm^{-1} in the UV range. Typical laser pulse energies in the probed volume are in the 50–250 μJ range for most of the species. The dye laser pulse is 10 ns in duration and the laser beam waist is about 600 μm in diameter for the metal detection and 1 mm in diameter for carbon detection (Fig. 1). The power density at the probe volume is at maximum 8 MW/cm^2 for all species except for C_3, where it reaches about 20 MW/cm^2.

TABLE I. Boiling and melting temperatures of pure metal and melting temperatures of metal-carbon (M-C) alloys. The formation temperature of the stable metal carbide (M_xC_y) for Fe and Y are reported in the last column.

	Gas↔Liquid	Liquid↔Solid	M-C (C at. %)	M_xC_y
Metal	$T_{boiling}$ [a] (K)	$T_{melting}$ [b] (K)	$T_{eutectic}$ [b] (K)	$T_{formation}$ [c] (K)
Fe	3023	1811	1426 (17.3)	1525 (Fe_3C)
Ni	3003	1728	1599.6 (8)	
Co	3143	1768	1593 (11.6)	
Y	3610	1795		2563 (YC_2)

[a]Temperature corresponding to a saturated vapor pressure of 1 bar from *Handbook of Chemistry and Physics*, 66th ed., edited by R. C. Weast, (CRC Press, Florida, 1985–1986), p. D-215.
[b]H. Okamoto, *Phase Diagrams for Binary Alloys* (Desk Handbook, ASM International, 2000).
[c]H. Okamoto, J. Phase Equilibria **13**, 543–565 (1992).

The induced fluorescence radiation is collected at right angle to the laser beam axis by a 60 mm focal length lens coupled to an optical fiber, 1 mm in diameter, with a magnification of 1. Therefore, the resolution is 1 mm along the target radius. The fluorescence is filtered by means of a spectrometer (Jobin-Yvon, H-20) equipped with a 1 mm wide exit slit, providing 4 nm spectral resolution, or with a 2 mm slit, providing a 8 nm resolution for C_3. The signal is detected by a photomultiplier tube (Photonis, XP2018B in UV and XP2017B in visible). The output signal is integrated over the temporal gate of 180 ns and averaged using a Boxcar system (Stanford Research, SR 250). The resulting signal is monitored with a digital oscilloscope (TDS 3052, 500 MHz, Tektronix). The dye laser beam is aligned in front of the LIF collection optics with an accuracy of ± 150 μm by using a retroalignment procedure. In this procedure, part of the laser light is passed through the detection optics and its spot is superimposed onto the incoming laser beam axis.

The UV range was first chosen to avoid interference with the blackbody radiation produced by the heated target and located in the first millimeter above the target.[18,21] A noticeable reduction in that interference was obtained in the spectral range (200–450 nm) and in the spatial range (600 μm to 20 mm). Spectral filtering is readily achieved by means of the spectrometer. However, the blackbody radiation produces a continuous background of about 60 photoelectrons at 400 nm and T_s=3500 K,[21] which is efficiently filtered by the temporal gate of the Boxcar system. The scattered laser light measured over the cold target has a residual level of about 2–10 photoelectrons at h=0.6 mm, but is larger over catalyst-doped targets, especially when iron is used. It is totally suppressed when the vaporization process starts since the hot carbonaceous flow dumps the scattered laser light. We have also checked that absorption of the dye laser beam by the hot flow is negligible at 248 and 430 nm (less than 2%). Let us recall here that the LIF signal is proportional to the population of the ground level of the electronic transition excited by the laser. Each species possesses particular transitions offering strong enough intensity so that the LIF signal is easily detected. The choice of the transition is presented in the spectroscopic section of the following paragraphs. In the thermodynamic conditions of the reactor, a careful check of the linear behavior of the signal as a function of laser energy is performed on the selected electronic transitions. Spectral investigations are performed at T_s=3200, 3300, and 3500 K with experiments lasting from 20 min to 7 min, respectively. By recording the vaporization conditions over different runs, as specified in Sec. II (Fig. 2), it is possible to check that stable conditions of target temperature lead to longer runs. On the other hand, instabilities due to protuberances shorten the vaporization process.

A. C_2 and C_3 detection

1. Carbon dimers

a. Spectroscopy. The C_2 Swan bands are known to lie in the visible range; extensive literature provides us with fine rotational structures of the vibrational bands of the $a\ ^3\Pi_u - d\ ^3\Pi_g$ electronic system.[23–25] Calculation of the spectra is performed using the computer code LASKIN provided by Kohse-Hoïnghaus *et al.*[26] from the University of Bielefeld. The spectral domain investigated in the present study covers the cold and hot bands ranging from 436 to 439 nm.

LIF is used to investigate the distribution of C_2 in the flow. The blue laser beam is attenuated in order to prevent saturation of the strong (2–0) band head located at 438.2 nm.[27,28]

Most of the C_2 LIF excitation spectra are recorded at 1.2 mm above the target (T_s=3200 K). The detection window is set at 469 nm [Fig. 4(a)] and the laser wavelength is tuned over 2 nm at a speed of 0.001 nm/s. The laser bandwidth is 0.08 cm^{-1}. The cold band (2–0) and two hot bands (3–1) and (4–2), i.e., originating, respectively, from vibrational levels v=0, 1, 2, are observed. They overlap due to the large number of rotational levels populated at that temperature. A calculated spectrum, shown in Fig. 4(b), assumes that the vibrational and rotational temperatures are equal. The gas temperature is assumed to be 2350 K as measured by CARS at h=1.2 mm for T_s=3200 K.[14] The calculated relative intensities of the (2–0) and (3–1) bands are in good agreement with the measured ones. The third (4–2) band is seen to not agree very well. It should be recalled here that after 20 min of run which is necessary to record the two first bands, the regime of vaporization becomes unsteady owing to the for-

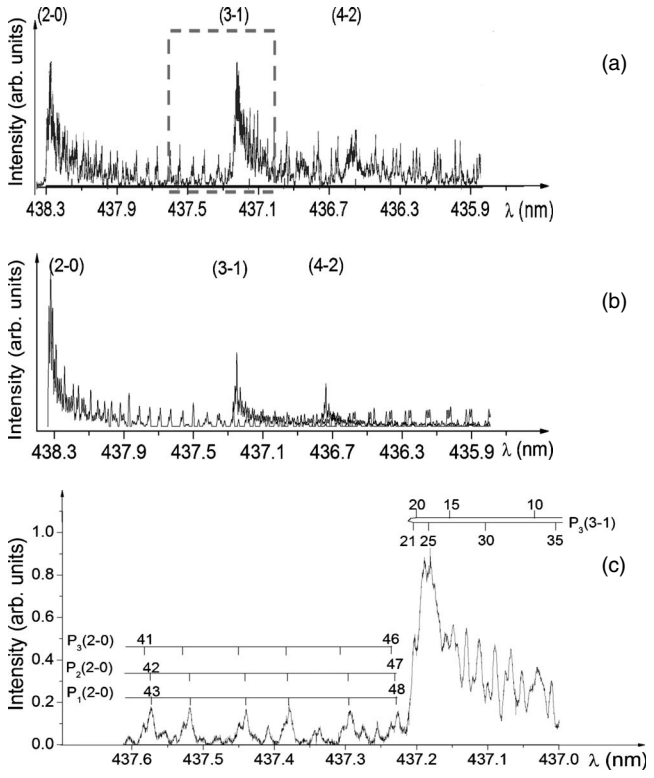

FIG. 4. (a) Excitation spectrum of C_2 Swan system recorded at 1.2 mm above a C:Co:Ni target at T_s=3200 K in He (300 hPa, 50 ml s^{-1}). Detection at 469 nm (bandwidth=4 nm). Three vibrational bands, (2–0), (3–1), and (4–2) are observed. (b) Calculated spectrum. We have assumed that the rotational and vibrational temperatures are in equilibrium with the He gas temperature equal to 2350 K at h=1.2 mm as measured by CARS (see Fig. 3). (c) Part of the excitation spectrum [dashed zone in (a)] is also recorded vs height above the target in Fig. 7. The prominent P rotational lines are assigned according to the data from Ref. 23.

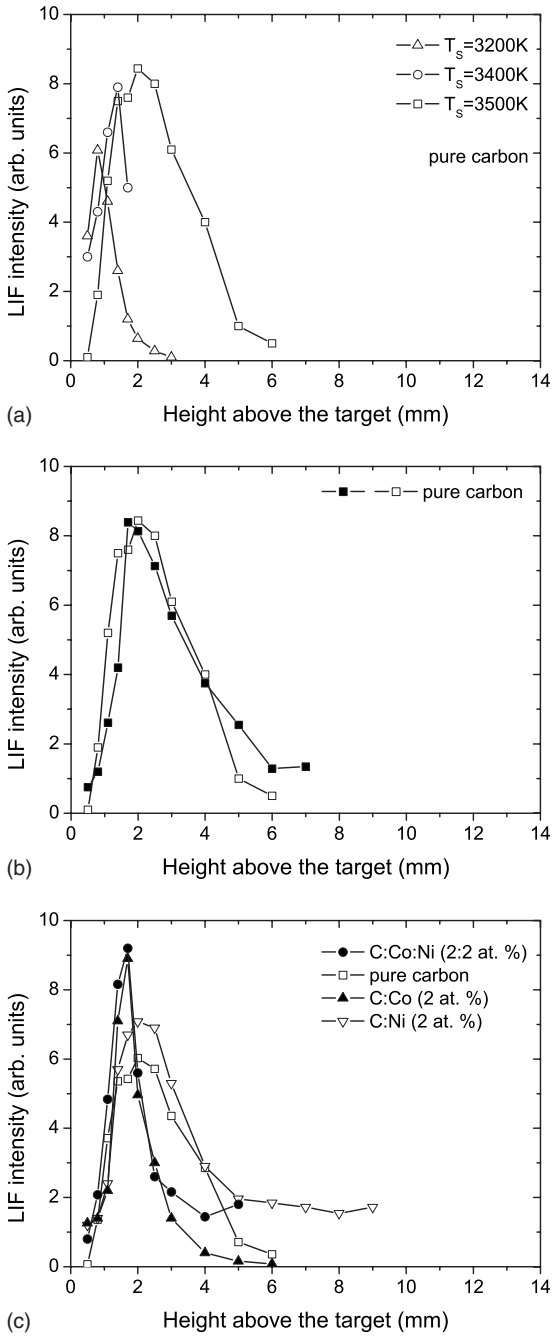

FIG. 5. (a) Spatial evolution of LIF signal of C_2 (2–0) for a pure carbon target at various T_s. (b) Two profiles measured at T_s =3500 K are given for repeatability. (c) For various target compositions at T_s=3500 K.

mation of protuberances on the target surface that affects the measured third band (4–2) in intensity and shape.

b. Spatial profiles. Spatial explorations of the hot flow are carried out by translating the laser beam axis above the target with a translation stage having a relative position accuracy of 1 μm. The laser beam spot is monitored during each vertical scan of the laser to control its location relative to the target which is also translated during the run so that its surface is staying in the same horizontal plane. The zero reference in height corresponds to the position at which the laser spot is a half shadowed by the target. The accuracy of this zero reference is ± 150 μm. The zero height is systematically checked before and after each vertical scan. It can vary by at most 400 μm after a vaporization run of 15 min. The laser beam and the detection lens are translated in steps of 300 μm near the target to correctly resolve the C_2 vertical profiles which are rather narrow. The resulting profiles obtained for different target temperatures and for various target compositions are displayed in Figs. 5(a) and 5(c), respectively. Figure 5(a) shows that the peak of C_2 signal occurs at 0.7, 1.3, and 2.0 mm above a pure carbon target for 3200 K, 3400 K, and 3500 K, respectively.[18]Although the profile behavior is reasonably well reproduced experimentally over different targets, the absolute amplitude of the signal is slightly dependent on the target surface quality, (pits and scratches). Since vertical profiles are recorded in about 3–5 min at 3500 K, the change in the target surface quality may affect the LIF signal during profile recording. Accordingly, the profiles are reproduced several times to take into account that effect and to check the repeatability of the measurements. The reproducibility of the shapes of the profiles is checked in Fig. 5(b) by comparing two runs over pure carbon targets at T_s=3500 K. The shapes and intensities are rather repeatable for all compositions and temperatures of the target.

The shift of the C_2 peak position with increasing temperature reveals the expansion of the vaporized carbon plume and the vaporization layer as the vaporization laser power is enhanced. In the vaporization layer, carbon vapor is in thermodynamic equilibrium with the surface (the partial pressure at the surface is equal to the vapor pressure at equilibrium). Accordingly, even at such temperatures (3000–3500 K), carbon evaporates from the surface. Several molecular species and metal atoms are probably formed in this layer in their ground as well as in their excited electronic states. Let us recall that the C_2 Swan system involves a lower electronic-state a $^3\Pi_u$ lying 1500 cm^{-1} above the ground state. The LIF signal of C_2 is not detected inside the vaporization layer whatever the temperature probably because the population of the $^3\Pi_u$ state is too low in this layer. We can speculate that C_2 and other species are highly electronically excited in the vaporization layer. C_2 may be formed in excited states through recombination from C atoms and collisional dissociation of large clusters.[29] Photodissociation of fullerenes and carbon clusters may also occur during the strong interaction of CO_2 laser with the target.[30] Also, the incoming CO_2 laser (Fig. 1) with a wavelength of 10.6 μm (corresponding to 950 cm^{-1}) can pump directly C_2 in higher energy states through a multiphoton excitation process.

C_2 signal increases when the population of excited electronic states is redistributed by relaxation toward the lower a $^3\Pi_u$ state. The LIF signal reaches a maximum outside of the vaporization layer, which indicates that the C_2 dimer is actually formed in this layer, as expected from chemical kinetic modeling.[20]

In Fig. 5(a), the vaporization layer thickness is seen to increase with increasing target temperature. At T_s=3500 K, the C_2 profile is seen to extend farther away from the target as a result of the expanded size of the carbon cloud which is blown away from the target as the CO_2-laser power increases.

In Fig. 5(c), at T_s=3500 K, the profiles obtained over pure carbon and C:Ni targets are rather similar in shape. C_2 is easily detected between 1 and 4 mm and the bell-like shape of the profile is ending around 4 mm. It thus indicates that C_2 disappears at the end of the thermal region 1 (Fig. 3). Region 1 is thus confirmed to correspond to the location where primary condensation of carbon takes place (fast cooling). The segregation of carbon as regards to Co catalytic effect is described in the following paragraph.

The behavior of C_2 is not the same with Co catalyst in the target. Over C:Co and C:Co:Ni targets, the profile is narrower and reaches a two times higher maximum located at 1.7 ± 0.15 mm. Immediately after that maximum, the profile exhibits a steep decrease between 2 and 2.5 mm. As a result, the C_2 signal is smaller by a factor of 3 at h=4 mm compared to the signal recorded over the pure carbon and C:Ni targets. This observation clearly indicates that the depletion of C_2 is far much faster when cobalt is present into the gas phase. It suggests that a recombination process between C_2 and Co may occur to form the CoC_2 radicals or small $Co\text{-}(C_2)_n$ clusters.[21] This reaction of cobalt with carbon dimer will be supported by an other observation of Sec. III B since cobalt atoms are not remaining in the gas phase as long as nickel atoms.

The evolution of the C_2 signal was also measured at h =1.2 mm vs target temperature (between 2800 and 3600 K).[18] The C_2 LIF signal is plotted vs inverse temperature in Fig. 6 to check whether it follows an Arrhenius behavior. This signal variation can be compared to the variation in the vaporization velocity measured in Fig. 2(b). From the slope of the C_2 line, an activation energy of (781 ± 36.5) kJ mol^{-1} is found which compares fairly well with the value (875 ± 78.9) kJ mol^{-1} measured from solid carbon weighting.

c. Vibrational populations and temperature. The degree of vibrational excitation of C_2 in the a $^3\Pi_u$ state has been probed. The intensities of the (2–0) and (3–1) Swan bands are measured in the excitation spectrum displayed in Fig. 4(c). This portion of the spectrum is composed of P, R lines belonging to the (2–0) band tail involving high rotational quantum number (i.e., $J \geq 41$), and to the (3–1) band head.

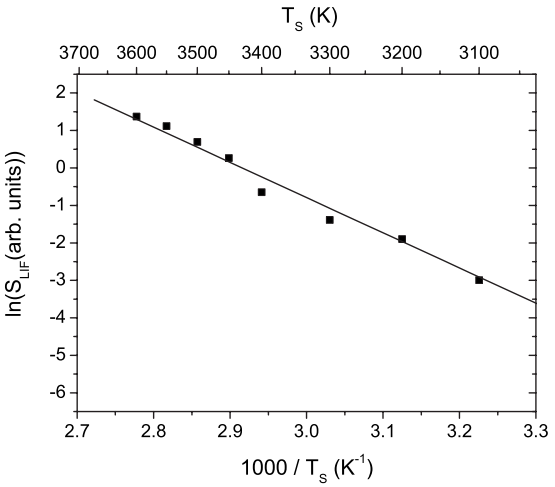

FIG. 6. LIF signal of C_2 vs inverse of T_s measured at 1.2 mm above a pure carbon target.

By recording this part of the spectrum above the target heated at 3200 K, the population ratio of the vibrational levels $v''=1$ and $v''=0$ can be probed vs height. Figure 7 compares that population ratio for a carbon target and a C:Co:Ni target.

Above a carbon target, the depletion of the excited ($v''=1$) state population occurs regularly beyond $h=2$ mm. However, on the doped target, the vibrational excitation seems to be shifted upwards. On that plot, the increase in vibrational temperature is evaluated to be about 2500 K (corresponding to 0.2 eV). This increase is maximum at $h=2$ mm and vibrational excitation of C_2 disappears at $h=3$ mm (Fig. 7) together with C_2 signal (Fig. 5). In this case, Ni and Co atoms are both present in the gas phase (see Sec. III B 2). One can assume that C_2 plays the role of an early energy carrier radical until $h=3$ mm where carbon and metal start to interact in different ways in order to form larger radicals or small clusters still very small since just forming in that part of region 1 (ending at $h=3.5$ mm in Fig. 3). Such a strong vibrational energy transfer is probably due to cobalt itself since Co atoms are assumed to strongly interact with C_2 as observed on the spatial profiles of Fig. 5(c).

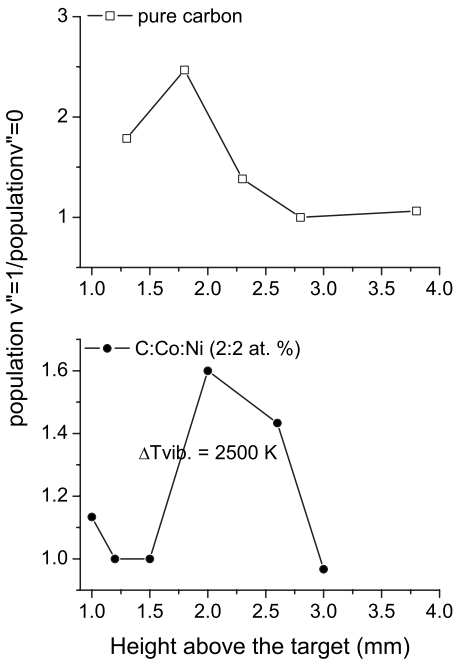

FIG. 7. Ratio of the populations of the vibrational states $v''=1$ and $v''=0$ of $C_2(a\ ^3\Pi_u)$ vs height above pure carbon (top) and C:Co:Ni (bottom) targets at $T_s=3200$ K in He (300 hPa, 50 ml s^{-1}). (The corresponding variation in vibrational temperature between 1.5 and 2 mm, denoted by ΔTvib., is indicated at bottom).

In summary, these results indicate that the primary condensation of carbon takes place in the 2–3 mm region, that is, in the region of fast cooling [region 1 in Fig. 3(b)]. At the end of this region, the C_2 signal vanishes indicating that most carbon atoms of the vapor phase are already recombining. Therefore region 1 can be defined as the region where the primary condensation of carbon takes place. Furthermore, within the vaporization layer (1–2 mm above the target),the C_2 radical is found to be mainly formed in excited electronic and vibrational states. It is shown that the depletion of the C_2 signal is accelerated by Co catalyst indicating the existence of strong interactions between the radical and this metal leading to the possible formation of CoC_2 radicals or small Co-C clusters. A main difference between the Ni and Co catalyst effect is thus evidenced here in the gas phase by the C_2 behavior.

2. Carbon trimers

The LIF investigation of carbon trimer is performed by monitoring the well-known Comet bands ($A\ ^1\Pi_u - X\ ^1\Sigma_g$) lying in the blue range around 405 nm.[31–35] In our study, C_3 is excited at 432.8 nm, corresponding to the vibrational bands (000)–(300) and (000)–(400) of the A-X transition.[34] A quasicontinuum is observed which extends from 426 to 440 nm since in the hot gas (3200 K), a large number of closely spaced rovibronic levels overlap, thus the fine structure is not resolved. Vertical profiles of fluorescence are measured by setting the detection window at 405 nm, corresponding to the cold band (000)–(000).[34] The width of detection window is 8 nm and the laser energy is 1.5 mJ in order to achieve a good signal/noise ratio. The spatial position of the probe volume is translated in steps of 300 μm, as for the C_2 measurements.

The profiles are obtained for various target compositions and for $T_s=3200$, 3400 and 3500 K [Figs. 8(a) and 8(c)]. The repeatability of the spatial measurements is shown in Fig. 8(b). The profile slightly changes with target composition since the LIF signal is stronger with catalyst than with pure carbon target [Fig. 8(a)]. The C_3 density peaks at $h=2$ mm and extends over 4 mm, thus confirming that carbon condensation starts in region 1 [Fig. 3(b)]. The signal peak is shifted when T_s rises from 3200 to 3500 K [Fig. 8(c)], as was observed for C_2 [Fig. 5(c)]. Here again, the vaporization layer thickness is seen to increase with increasing T_s. At $T_s=3500$ K, the C_3 profile extends farther away from the target surface due to enhancement of the vaporization process which is observed at higher laser power. As for C_2, C_3 concentration is larger when the catalysts are present and rapidly

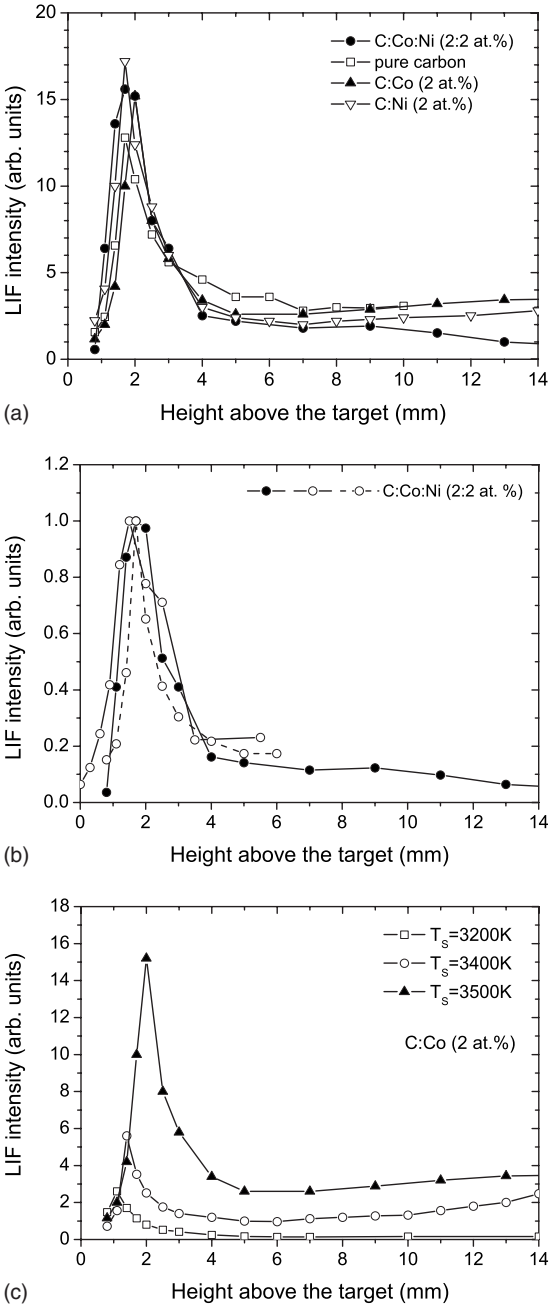

FIG. 8. (a) Spatial evolution of LIF signal of C_3 for various target compositions at T_s=3400 K. (b) Three measured profiles are given for repeatability. (c) For a C:Co target at various T_s.

vanishes at the end of the thermal region 1 [Figs. 3(b) and 8]. However, the behavior of C_3 does not depend on the nature of metal atoms, in opposition to the observation on C_2 [Fig. 5(c)]. Therefore, carbon trimers may not interact with metal species but do contribute to the growth of the carbon cluster.

From signals of Figs. 5(c) and 8(a), an attempt was made to estimate the ratio of the C_3 to C_2 number density, for a C:Co:Ni target at T_s=3500 K. To calculate the corresponding ratio, the following expression SLIF of LIF signal is used,[27]

TABLE II. Parameters used to estimate the ratio of the C_3 to C_2 number density according to Eq. (1) (see Sec. III A 2).

Species	C_3	C_2
Electronic system	Comet	Swan
	$A\ ^1\Pi_u - X\ ^1\Sigma_g^+$	$d\ ^3\Pi_g - a\ ^3\Pi_u$
F_B (%)	~2 [a]	~40 [e]
f_{osc}	0.033[b]	1.18×10^{-3} [f]
F_{fluo}	0.9[c]	0.4[g]
Y	0.11[c]	0.36[c]
E_{laser} (mJ)	1.5	0.3
S_{PM} (mA W^{-1})	11[d]	13[g]
$T_{spectro}$ (%)	40	45

[a]At 2500 K, G. A. Raiche and J. B. Jeffries, Appl. Phys. B **64**, 593–597 (1997).
[b]At 432 nm, D. M. Cooper and J. J. Jones, J. Quant. Spectrosc. Radiat. Transfer **32**, 201–208 (1979).
[c]Reference 27.
[d]At 400 nm.
[e]At 2500 K.
[f]At 438 nm, band (2–0), D. M. Cooper and R. W. Nicholls, Spectroscopic Letters **9**, 139–155 (1976).
[g]At 470 nm.

$$S_{\mathrm{LIF}} \propto N_{tot} \times F_B \times f_{osc} \times F_{fluo} \times Y \times E_{laser} \times S_{PM} \times T_{Spectro} \times (\Omega_c/4\pi) \times V_{probe}. \quad (1)$$

This relation is valid in the case of a linear dependence of the fluorescence signal on the laser intensity. N_{tot} (cm^{-3}) is the total number density. F_B is the Boltzmann fraction of the molecules in the probed level and depends on the gas temperature. f_{osc} is the absorption oscillator strength of the electronic transition involved in LIF excitation process. F_{fluo} is the fraction of fluorescence detected in the spectral window of the spectrometer. Y is the fluorescence quantum yield which accounts for both radiative and collisional deactivation of the electronic excited levels. E_{laser} (mJ) is the laser energy at the probe volume. S_{PM} (mA W^{-1}) is the radiant sensitivity of the photomultiplier tube at a given wavelength. $T_{spectro}$ (%) is the transmission efficiency of the spectrometer in the fluorescence window. Ω_c (sr) is the solid angle of fluorescence collection. V_{probe} (cm^{-3}) is the probe volume defined by the overlap zone between the laser beam and the collection sample. Table II gives the parameters relative to C_3 and C_2, respectively, excited in the Comet and Swan systems. Let us remark that the geometric factor ($\Omega_c/4\pi \times V_{probe}$) is unchanged for C_3 and C_2 analysis so that it is not taken into account in the calculation. The signal ratio is estimated to be 1.5 at h=1.7 mm where the gas temperature is assumed to be 2500 K (Fig. 3). The corresponding ratio of C_3/C_2 number density is estimated to be 10^{-2} by taking into account the parameters given in Table II. This ratio is equal to 15 in the thermodynamic calculations of carbon species evaporated from carbon at about 2000 K.[36] The large excess of signal from C_2 that we observed may be due to highly enhanced formation of C_2 whereas C_3 mainly originates from regular carbon condensation.

In summary, over the 3 mm of region 1, metal addition seems to enhance carbon radicals formation since the carbon

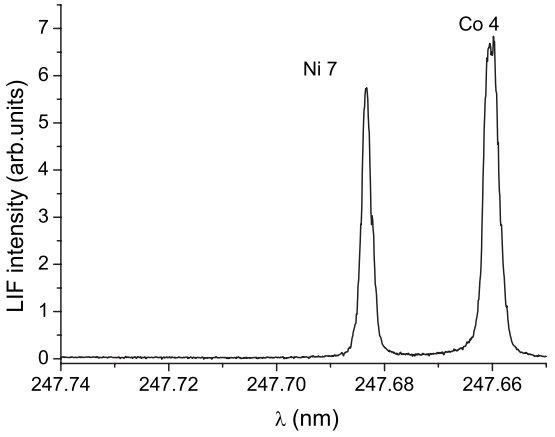

FIG. 9. Excitation spectrum recorded at 4 mm above a C:Co:Ni target at T_s=3200 K in He (300 hPa, 50 ml/s). Detection at 350 nm (bandwidth=4 nm). Two lines are observed: line 7 of Ni and line 4 of Co (see Table III for spectroscopic data).

condensation process is changed when metal catalyst is present. It seems to act in favor of C_2 production. This effect will be further studied in Sec. V.

B. Detection of Ni and Co atoms

1. Spectroscopy

The spectral lines due to Ni, Co, and Fe have been identified in the LIF spectra previously presented in Ref. 18. The laser wavelengths used for monitoring the metal atoms extend between 247.5 and 248 nm. It was demonstrated that the strongest and most discriminating fluorescent emission from Ni, Co, and Fe are located at 338 nm, 350 nm, and 301 nm, respectively.[18] The exit slit of the spectrometer is set to these spectral windows for detecting the signals originating from these metallic species and for scanning excitation spectra. A portion of the excitation spectrum composed of nickel and cobalt lines is shown in Fig. 9. Spectroscopic data relative to these lines, numbered 7 and 4, are given in Table III. Let us note that nickel and cobalt atoms have been already detected by De Boer *et al.*[37] and by Puretzky *et al.*[4,16,38] in a pulsed laser ablation process.

2. Spatial profiles

The region between the target and the silica tube is investigated in steps of 500 μm, nearly equal to the beam diameter (Fig. 1). A steep change in the signal near the target surface is sometimes investigated with better resolution, in steps of 300 μm when necessary. This experimental procedure enables vertical distribution in the gas phase of the metal atoms to be measured with both a good accuracy and reproducibility as for C_2 and C_3.

Targets composed of C:Co (98:2 at. %), C:Co:Y (94.8:4.2:1 at. %), C:Ni (98:2 at. %), and C:Co:Ni (96:2:2 at. %) have been vaporized in order to observe specific behavior relative to nickel and cobalt. In Figs. 10 and 11, respectively, the LIF signals of nickel (line 7) and cobalt (line 4) (Table III and Fig. 9) are plotted vs height above the target at T_s=3500 K, in the flow conditions given in Sec. II. Although the profile behavior is reasonably well reproduced experimentally over different targets, the absolute amplitude of the signal is slightly dependent on the target surface quality (pits and scratches). Since vertical profiles are recorded in about 3–5 min at 3500 K, the change in the target surface quality may affect the LIF signal during profile recording. Accordingly, the profiles are reproduced several times to take into account that effect and to check the repeatability of the measurements. Examples of repeatability are shown for Ni and Co profiles in Figs. 10(b) and 11(b), respectively. The relative accuracy of the fluorescence measurements of Ni and Co is estimated to be 30% according to the signal fluctuation (rms) measured over 100 laser shots.

As for C_2 and C_3 radicals, no signal is detected in the vaporization layer up to 1 mm above the surface target. Since LIF signal originates from atoms probed in their ground or low-lying electronic states (Table III), it appears here again that, as for carbon radicals, metal atoms are strongly pumped into highly excited electronic states as a result of CO_2-laser irradiation (multiphoton excitation) and kinetic excitation processes (collisional recombinative and dissociation processes of small clusters). This interpretation is supported by the strong atomic emission observed within this layer and duly assigned to metal bands in our previous study.[21] The emission results from fast de-excitation of these excited states down to the lower electronic states. Beyond the first millimeter above the target surface, as for carbon species, the

TABLE III. Identification of the observed excitation lines of Ni, Co, and Fe atoms. Spectroscopic data are from atomic spectral line database from CD-ROM 23 of R. L. Kurucz, P. L. Smith (a), C. Heise (b), J. R. Esmond (a) [(a) Harvard-Smithsonian Center for Astrophysics, (b) Deutsche Telekom AG, Product Center Business Multimedia (PBM)]: wavelength in air, λ_{air}; wave number in vacuum, ω; absorption oscillator strength, f; transition probability for spontaneous emission, A; energy and statistical weight of the lower state, E_i and g_i, and of the upper state, E_k and g_k.

Atom	Line No.	λ_{air} (nm)	ω (cm^{-1})	f	A (s^{-1})	E_i (cm^{-1})	g_i	Label	E_k (cm^{-1})	g_k	Label
Fe	4	248.327	40257.307	5.57×10^{-1}	4.93×10^{8}	0.000	9	$a\ ^5D_4$	40257.307	11	x $^5F^0_5$
Ni	5	248.190	40279.496	6.67×10^{-5}	1.01×10^{5}	204.786	7	$a\ ^3D_3$	40484.282	5	$^5P^0_5$
Fe	6	247.997	40314.046	1.70×10^{-1}	1.5×10^{8}	704.004	5	$a\ ^5D_2$	41018.050	5	x $^5F^0_5$
Ni	7	247.687	40361.254	1.84×10^{-3}	2.58×10^{6}	0.000	9	$a\ ^3F_4$	40361.254	7	$^5P^0_3$
Co	4	247.663	40365.160	1.58×10^{-2}	2.15×10^{7}	3482.820	10	$b\ ^4F_{9/2}$	43847.980	8	$w\ ^4F^0_{7/2}$

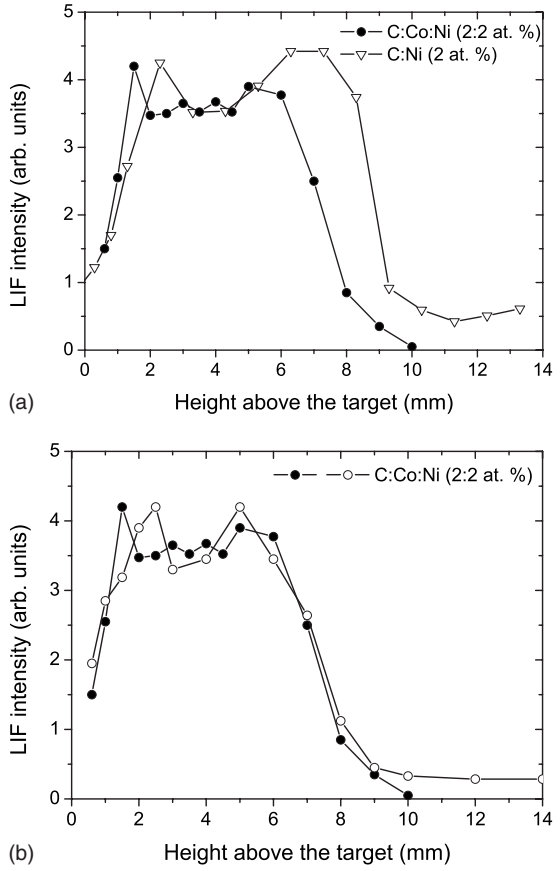

FIG. 10. (a) Spatial evolution of LIF signal of Ni (line 7) for C:Co:Ni and C:Ni targets at T_s=3500 K in He (300 hPa, 50 ml s^{-1}). (b) Two measured profiles are given for repeatability.

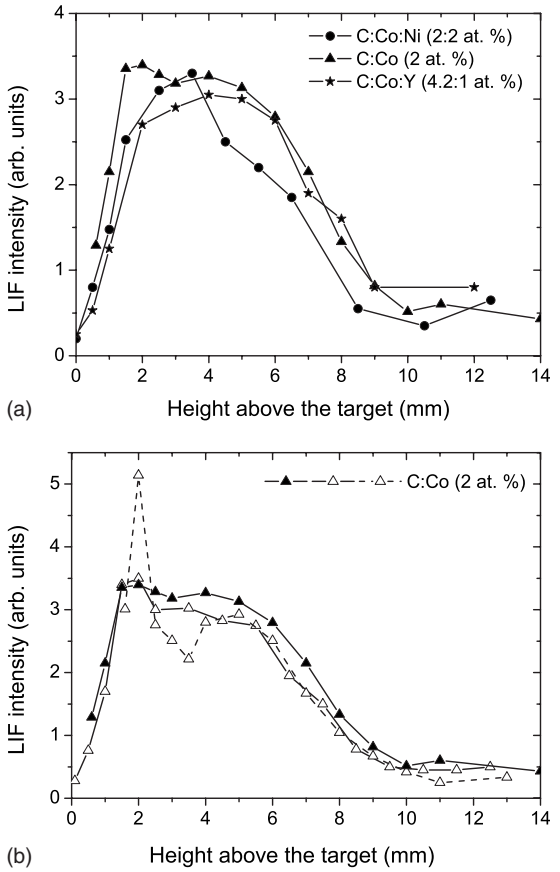

FIG. 11. (a) Spatial evolution of LIF signal of Co (line 4) for C:Co:Ni, C:Co, and C:Co:Y targets at T_s=3500 K in He (300 hPa, 50 ml s^{-1}). (b) Three measured profiles are given for repeatability.

LIF signal sharply increases and reaches a peak between 1.5 and 2 mm (Figs. 10 and 11). Then, the signal levels off between 2 and 6 mm and finally vanishes at about 8 mm, that is at the end of region 2 of the temperature gradient (Fig. 3). The vanishing of the LIF signal means that metal atoms have disappeared from the gas phase and are fully condensed into liquid or solid clusters and particles. Therefore the region 2 of the temperature gradient can be defined as the region where the metal gas transforms into a condensed (liquid and solid) phase. The way this phase transformation occurs, is revealed by the LIF profile which exhibits a peculiar behavior in the form of a more or less extended plateau. Assuming that the metal particles are surrounded by a cloud of supersaturated metal vapor, one can calculate the equilibrium vapor pressure of both Co and Ni as a function of temperature by using the temperature profile measured in Fig. 3. It is worth mentioning that the temperature at the end of region 2 is close the eutectic temperatures of Ni-C and Co-C systems. Our results therefore indicate that metal gas phase disappears at a temperature close to the solidification point of metal particles.

The thermodynamic calculation shown in Fig. 12(a), reveals that at equilibrium a continuous decrease in metal vapor pressure is expected.[21] This behavior is obviously not observed from Co and Ni signals. The metal vapor pressure has to be calculated by taking into account for the dynamics of the gases, metal carbon reactions in the gas phase, and the subsequent formation of metal-C clusters. This calculation has been done using the chemical kinetic code developed by Scott for our experimental conditions and target compositions. The results of the calculations are detailed in Ref. 21 but some of them require a deeper interpretation and comparison with other results presented here. In the chemical kinetic model, the evolution of metal atoms is mainly driven by the condensation/evaporation routes of metal clusters interacting with carbon at different stages of the synthesis.[20] The concentration of Ni and Co atoms in the gas phase results from the condensation/evaporation rates of Ni and Co clusters, which are based on the bond energy of the Ni-Ni and Co-Co dimers. According to the literature data, the bond energies were first assumed to be 203 kJ mol^{-1} for Ni-Ni and 167 kJ mol^{-1} for Co-Co dimers [www.webelements.com.data]. However, in the case of cobalt, the bond energy appears to be very uncertain (from 140 to 230 kJ mol^{-1}), and a value equal to 208 kJ mol^{-1} was retrieved by fitting measured and calculated Co profiles.[21] The final comparison of calculated and measured profiles is illustrated in Figs. 12(b) and 12(c). The calculations of Ni and Co atoms evolutions well reproduce the experimental LIF profiles, therefore demonstrating that the plateau is related to the extension of metal vapor around its liquid in supersaturation due to cooling condition in which gas dynamics plays the major role in contrast to static calculation of Fig. 12(a).

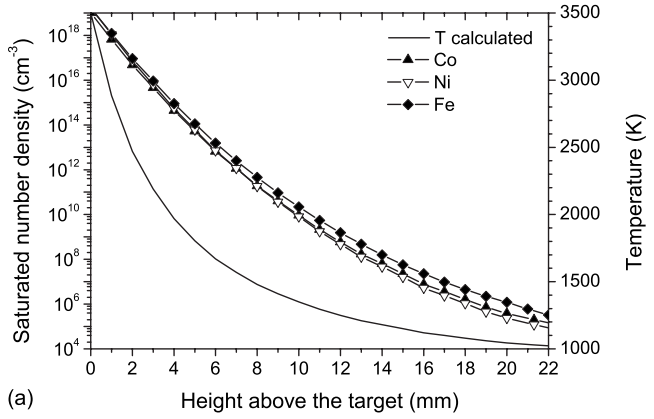

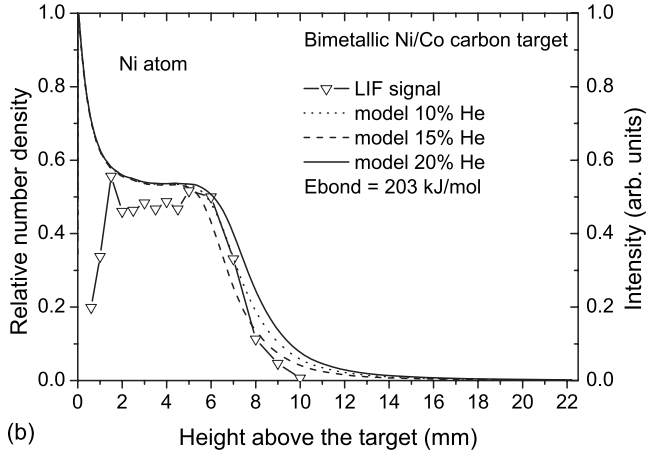

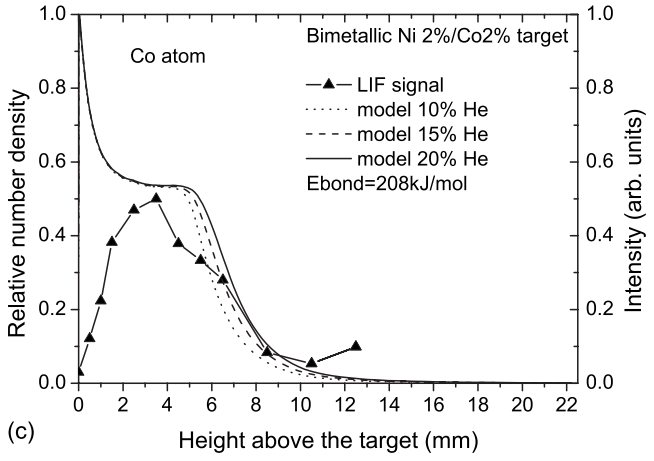

FIG. 12. (a) Calculated saturated number density of Co, Ni, and Fe vs height above the target at T_s=3500 K. Calculated temperature profile of Fig. 3 is reported (solid line). Metal vapor pressures are extracted from www.veeco.com/learning/learning_vaporelements.asp for pressures below 133 Pa and from Handbook of Chemistry and Physics, 66th ed., edited by R. C. Weast, (CRC press, Florida,1985–1986), p. D-215 for pressures above 133 Pa. [(b) and (c)] Comparison between measured and calculated evolutions of Ni and Co atoms, respectively. Measurements with a C:Co:Ni target at T_s=3500 K in He (300 hPa, 50 ml s^{-1}). Simulations obtained for 10%, 15%, 20% He dilution cases and by assuming a dimer bond energy of 203 kJ mol^{-1} for Ni-Ni and 208 kJ mol^{-1} for Co-Co.

However, thanks to the comparison with saturated number density, the absolute concentration of atoms can be estimated. The concentration of atoms (Ni and Co) drawn from the calculations is 3×10^{16} cm^{-3} at the plateau. It corresponds to the saturated-vapor density at 2300 K (h =2.5 mm), based on thermodynamic data [Fig. 12(a)].[21,22]

In Fig. 10(a), the length of the plateau of Ni vapor is seen to be different above a bimetallic C:Co:Ni (96:2:2 at. %) and a monometallic C:Ni (98:2 at. %) target. The location at which the Ni fluorescence decreases and disappears is shifted from 6–8 mm for the bimetallic target to 8–10 mm for the monometallic target. With nickel only, condensation appears later in the plume. Calculation of the condensation/evaporation process has evidenced the effect of metal dilution.[21] The metal is half diluted (2 at. % instead of 4 at. %) at the monometallic target and thus the cluster formation is delayed as evidenced by the calculated profiles which fit properly the measured ones.[21] When the fluorescence signal vanishes between 8 and 10 mm, the temperature has dropped to 1400–1200 K, and the metal condenses.[12] As a consequence, metal atoms disappear from the gas phase, the decrease in LIF signals reveals that the transformation of the molten nickel particles directly drives the flow composition. In the case of cobalt, the difference observed between bimetallic and monometallic C:Co targets is less pronounced since the fluorescence signal decreases between 4 and 6 mm whatever the target composition [Fig. 11(a)].

In any case, the Co signal decreases sooner than Ni signal. The higher dimer bond energy (208 kJ mol^{-1}) which is drawn from our calculation [Fig. 12(c)] will result in a faster coalescence of Co atoms to form clusters, as compared to the previous calculation with a dimer bond energy of 167 kJ mol^{-1}. The particular behavior of cobalt atom is attributed to a very fast agglomeration into Co-C clusters. The difference in bond energy (41 kJ mol^{-1}) drawn from Fig. 12(c) reveals that cobalt condensation is changed because Co atoms have already interacted with carbon prior to Co-Co dimer formation thus increasing the dimer bond energy of pure cobalt in the calculation. In Sec. III A, it was already assumed that Co may interact strongly with the carbon dimers, since the depletion of the C_2 signal was accelerated by the presence of Co into the gas phase [Fig. 5(c)]. Here, an additional evidence that a very early interaction takes place between C_2 and Co is given which can be reasonably associated with the ability of Co to promote the segregation of carbon at the surface of metal-carbon clusters. To further study the different behavior of Co and Ni, transmission electron microscopy (TEM) analysis of the metal particles found in the synthesized products is undertaken in the next section.

IV. TEM ANALYSIS OF METAL NANOPARTICLES

When the gas temperature drops, the resulting size of the liquid droplets is controlled by the cooling rate and can also be measured in the products. Figures 13(a)–13(c) show TEM images of the C:Co, C:Ni, and C:Fe nanoparticles. The samples with nickel contain small and large pure metal particles (round in shape) embedded in large amorphous carbon flakes. The sample with cobalt displays small particles

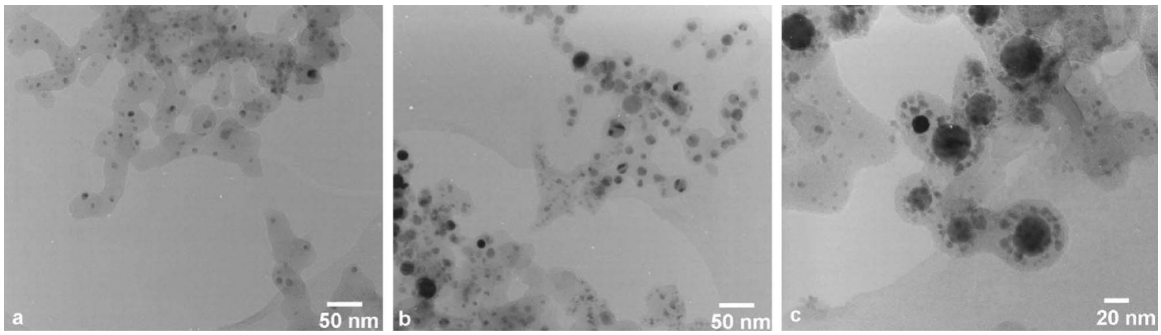

FIG. 13. TEM images of products obtained by laser vaporization of (a) C:Co (2 at. %), (b) C:Ni (2 at. %), and (c) C:Fe (2 at. %) targets at T_s=3500 K in He (300 hPa, 50 ml s^{-1}). Metal nanoparticles appear as dark spots.

(round in shape) in amorphous carbon with a uniform size distribution.

The diameters of the nickel and cobalt particles have been also estimated in TEM. Figures 13(a)–13(c) display histograms of the particle diameters in the monometallic C:Co, C:Ni, and bimetallic C:Co:Ni samples. They are obtained over at most 1165 particles by means of a processing software (IMAGEJ) of microscopy. Statistical analyses have been carried out over 5–9 TEM images by analyzing zones which are randomly chosen. The diameter of a metal particle which appears as dark spot in TEM images is measured by manual processing. It is worth noting that TEM is a sampling technique so that many particles, especially the small ones that are hidden by amorphous carbon, are missing in the counting. Accordingly, the statistics on small diameters are certainly underestimated. Nonetheless, the resulting histograms give a general trend of the size dependence on the nature of metal catalyst used alone or in pairs. The insets in Figs. 14(a)–14(c), display diameter distribution which is more "realistic" than an average value owing to the large disparity particle diameters. We find that the Co particles are actually the smallest ones, ranging between 5.5 and 8.5 nm, with a narrow dispersion from 2 to 18 nm. In contrast, Ni particles exhibit a broader distribution of diameters extending up to 70 nm. Most of the Ni particles have diameters lying between 3.5 and 10.5 nm. It is worth noting that the maximum (most probable) diameter in both distributions is 7 nm. In Ni-Co catalysts mixture [Fig. 14(c)], an intermediate size distribution is obtained with the most probable diameter in the 5–9.5 nm range. The significant difference between the size distributions of Ni and Co particles is consistent with some previous TEM observations of the solar furnace samples (Ni particle size of 50–100 nm and Co of 5–6 nm).[5] Finally, these results confirm our above-mentioned suggestions that condensation of Co proceeds differently than the one of Ni, due to an early interaction between Co and C occurring at the first stage of carbon condensation in region 1 of the thermal gradient (Fig. 3). A further investigation of size effect is performed in Sec. V.

In conclusion, the precipitation/segregation (dissolution/diffusion) mechanism is assumed to be the most probable process taking place on the edge of the right-hand side of the metal plateau [Figs. 12(b) and 12(c)].[5,11,12] Although molten clusters of Ni can be formed on monometallic and bimetallic targets of Fig. 10(a), carbon precipitates and segregates at the cluster surface with very different efficiencies when one or two catalysts are present in the plume. Segregation is faster with cobalt and dissolution of carbon is definitely faster with nickel.[5,11,12,39–43] Above C:Co:Ni (98:2:2 at. %) targets, segregation/precipitation/encapsulation may appear at T =1550 K when clusters reach the 10–20 nm size, consistent with the nucleation mechanism [step (b) in V-L-S model] proposed by Gavillet *et al.*[8,9] finding that the most likely particle diameter is about 15 nm.

V. LII ANALYSIS OF SOOT TRANSFORMATION

The LII technique was implemented to get detailed information about soot particle formation. This technique is commonly applied in combustion media.[19,44–48] This optical method is well suited to the analysis of carbon flow, particularly in the early stages of particle formation. However, the primary carbon radicals, C_2, C_3, C_4, …, which are considered as the precursors of soot, are too small to be probed by LII. As already discussed, the LIF technique is well suited to get information about these radicals. The initial composition of the carbon flow can also be predicted from chemical kinetic calculations.[49] Our first LII measurements were already presented in a previous paper.[18] In the present study, the location of the laser sheet with respect to the target surface is carefully imaged prior to each run in order to measure the absolute heights with good accuracy (80 μm). Furthermore, the same translation stage as for the LIF measurements is used in the present study so that the vertical LII and LIF profiles can be compared with the same degree of confidence.

The LII principle is to heat the sootlike particles with a pulsed laser beam and to collect the resulting transient blackbody emission from the laser-heated particles.[44] Under appropriate conditions, the LII signal is proportional to the soot volume fraction, and thus enables qualitative mapping of the soot particle distribution.[18] The particle diameter is deduced from the temporal shape of the LII signal, assuming particles with a spherical shape. The decay time of the LII signal is fitted using a model, assuming that heat conduction dominates the particle cooling process. The decay time depends on the particle size, the longer is the decay, the larger is the particle. LII enables the detection of soot particles ranging from few nanometers to about 100 nm in diameter. However, the particle size measurements are highly dependent on the

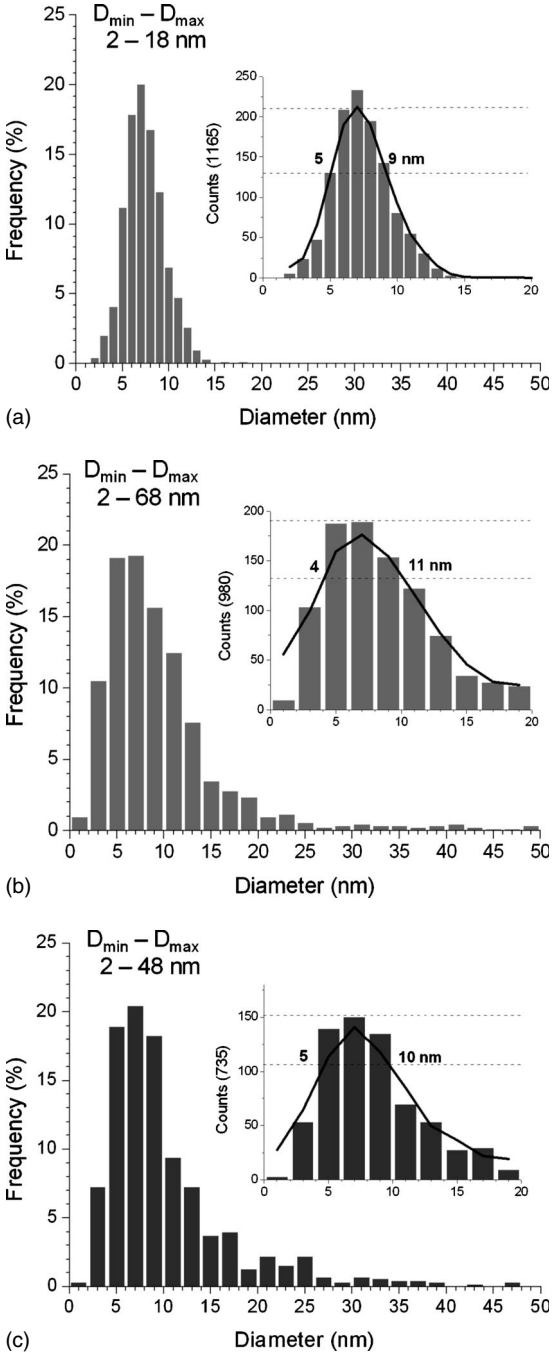

FIG. 14. Frequency histograms of the diameters of metal nanoparticles (bin size: 0.25 nm) retrieved from TEM images for (a) C:Co (2 at. %), (b) C:Ni (2 at. %), and (c) C:Co:Ni (2:2 at. %) targets. The inset on the right shows the number of counts vs diameter between 0 and 20 nm and the smoothing curve calculated over five points (solid curve).

type of LII models.[45] In our case, DLR-Stuttgart has developed a model which makes possible quantitative size measurements during our experiments. The uncertainty in the LII measurements of soot sizes is approximately 1 nm in the 5–25 nm range and 3 nm above 50 nm. The DLR team has obtained representative results in the cases of laminar sooting flames over a wide range of laser fluences[19,46] and successfully applied its know how in our reactor.

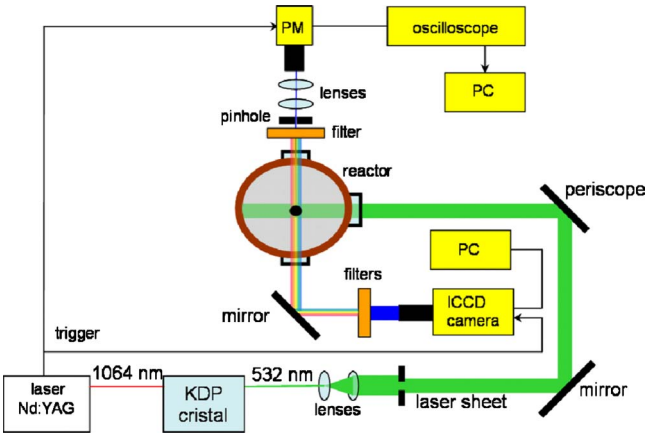

FIG. 15. (Color online) Experimental setup for LII measurements.

A. Experimental

The LII signal is generated using a frequency-doubled pulsed Nd:YAG laser (Quantel, YG 981C) which produces 532 nm emissions with 10 ns pulse duration and 10 Hz repetition rate (Fig. 15). Two kinds of measurements are performed: LII images of the probed volume are recorded on a charge coupled device (CCD) camera and the LII signal is monitored on a fast oscilloscope to analyze the temporal shape which allows size particles to be measured.

A laser sheet is formed using a cylindrical lens of 300 mm focal length and a spherical lens of 1000 mm focal length. Part of the laser sheet is selected to cover the area located between the target surface and the silica tube (Fig. 1). The probed volume of the hot flow is thus 20 mm $\times$ 20 mm $\times$ 290 μm. LII images are recorded with a gated intensified CCD camera enabling double exposure separated by a short delay (between 50 and 200 ns) in the range of the time scale of the laser-induced sublimation of soot. A first image is recorded without the laser and gives the background luminosity to be subtracted from the LII images, which are then recorded with the laser pulses on. It also accurately gives the location of the target. The temporal gate of the camera is set to 40 ns exposure time. The LII signal is detected 500 ns after the laser pulse in order to avoid any interference from fluorescence signals. Furthermore, the detection is spectrally filtered by means of an interference filter centered at 450 nm (450FS-40–50, LOT-ORIEL) and a dichroïc filter (B46, LINOS). The detection band pass is 20 nm wide. This spectral range was chosen out of the fluorescence range of carbon radicals such as C_2 (Swan bands) and C_3 (Comet band).[46] The repetition rate of the detection system lies between 2.5 and 5 Hz. The laser energy in the sampled map is about 10 mJ per pulse. The total image area is 43 mm $\times$ 54 mm with a resolution of 64 μm per pixel.

The temporal shape of the LII signal is measured using a photomultiplier tube (Hamamatsu, R928) (Fig. 15). The light is imaged onto a pinhole (0.8 mm in diameter) by means of two 300 mm focal length lenses (1:1 magnification). An interference filter centered at 400 nm with a 16 nm bandwidth (400FS20–50, Oriel) is placed in front of the photomultiplier tube to reduce the stray light. In addition, neutral density

filters are used to avoid saturation of the photomultiplier tube. The observation zone, which is 600 μm in diameter, can be translated above the target with the translation stage already used for LIF investigations, thus allowing similar vertical investigation of the laser sheet excitation volume. The zero reference position of the target is monitored by observing the occultation of the laser sheet by the far field of the laser beam.

The temporal evolution of the signal is recorded on a fast oscilloscope (TDS3034, Tektronix, 2.5×10^9 samples s^{-1}). The oscilloscope is triggered by a SRS pulse generator synchronized to the laser pulse. The signal is usually averaged over 524 pulses; and each acquisition is a set of 10 000 points, which corresponds to 4 μs. The LII signal lasts at most 1 μs in our pressure and temperature conditions.[18]

Primary particle sizing is achieved by comparing the measured and calculated temporal profiles. The DLR model accounts for (i) heating of the particle by absorption of the laser light, (ii) cooling by conduction into the ambient gas, (iii) radiative emission, and (iv) sublimation phenomena induced by the Nd:YAG laser pulse. That detection channel (Fig. 15) provides an independent measurement of the size of the carbon soot particle as a function of height into the vaporized plume.

Near the target surface, a spurious background is observed owing to the blackbody emission from the heated target. Proper subtraction of this background is performed in the final treatment of the temporal data. It is a source of uncertainty when the signal-to-noise ratio is too small.

B. Results

Sets of temporal evolution of the LII signal are recorded vs height. The spatial distributions of soot particle sizes obtained at $T_s=3400$ K and $T_s=3500$ K are shown in Figs. 16(a) and 16(b), respectively. With a pure carbon target, a linear increase in the size up to about 35 nm is obtained as a result of regular coalescence of carbon into larger soot particles. When metal catalysts are present, the soot never grows larger than 2–4 nm up to 5 mm above the target. This size corresponds to a lower limit of particles which can be detected by LII. Between 5 and 8 mm in height, above the target, a steep increase in the size of the soot to about 60 nm is measured; then a plateau is again observed beyond $h=8$ mm. The end of the plateau corresponds to the region where larger particles (>100 nm) are formed but cannot be detected anymore by LII. This limitation is responsible for the slight decrease in the signal which occurs at $h=19-21$ mm, that is just below the silica tube.

The maximum size of the soot which is measured optically is confirmed by *ex situ* scanning electronic microscopy (SEM) analysis of the products in which the mean size of carbon aggregates is estimated to be about 70 nm with a homogeneous size distribution [Fig. 16(c)]. So a main result is that peculiar nonlinear behavior is obtained when metal is present in the hot flow, especially at $T_s=3500$ K [Fig. 16(b)]. It reveals that a fast transformation of the soot takes place in the $h=4-8$ mm region, exactly in region 2 of the thermal gradient (Fig. 3).

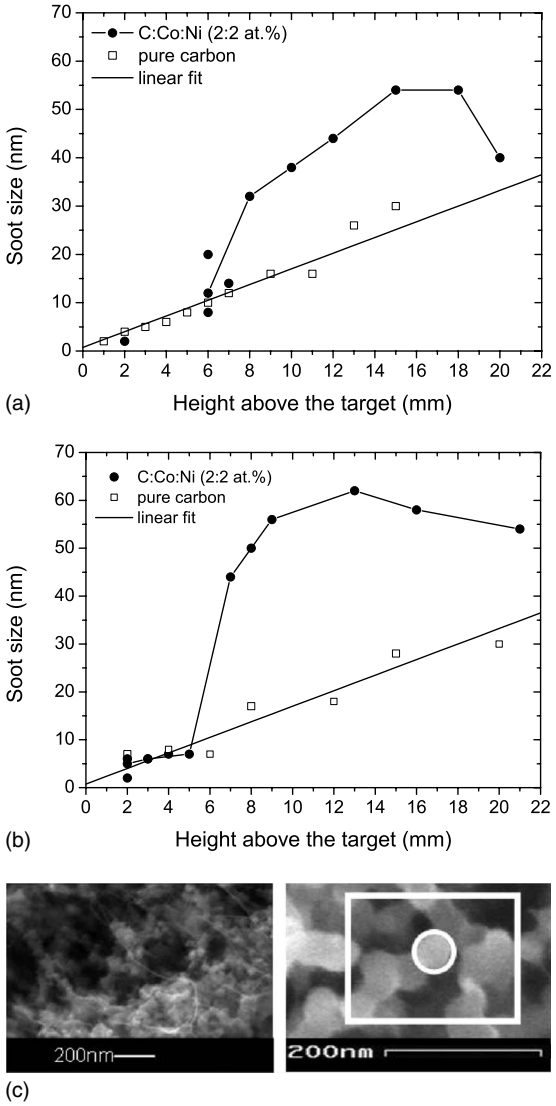

FIG. 16. Spatial evolutions of soot particles size measured by time-resolved LII in He (300 hPa, 50 ml s^{-1}) over C:Co:Ni and pure carbon targets at (a) $T_s=3400$ K and (b) $T_s=3500$ K. (c) SEM images of products obtained by laser vaporization of C:Co:Ni target at $T_s=3500$ K. The image at right shows a soot particle surrounded by a white circle [zoom (3×)].

Sets of 200 LII images are obtained in each sequence of 80 s. The run is synchronized with the recording of vaporization parameters. These digital images are averaged and a selection of them is shown in Fig. 17 vs temperature and target composition. The averaged images are well representative of each run but the absolute intensity given on vertical axis may change by less than 20% according to the target surface quality (area and density). During the first step of the vaporization process (20 s), the target area drastically increases as it is promptly etched by continuous CO_2-laser irradiation [Fig. 2(a)]. Experimental conditions become stationary when a uniform vaporization surface is well established. Optical recording is triggered at that step. The larger is the area, the stronger is the LII signal. If irregular protuberances are formed onto the target surface, turbulence is generated in the gas flow and accordingly disturbs the

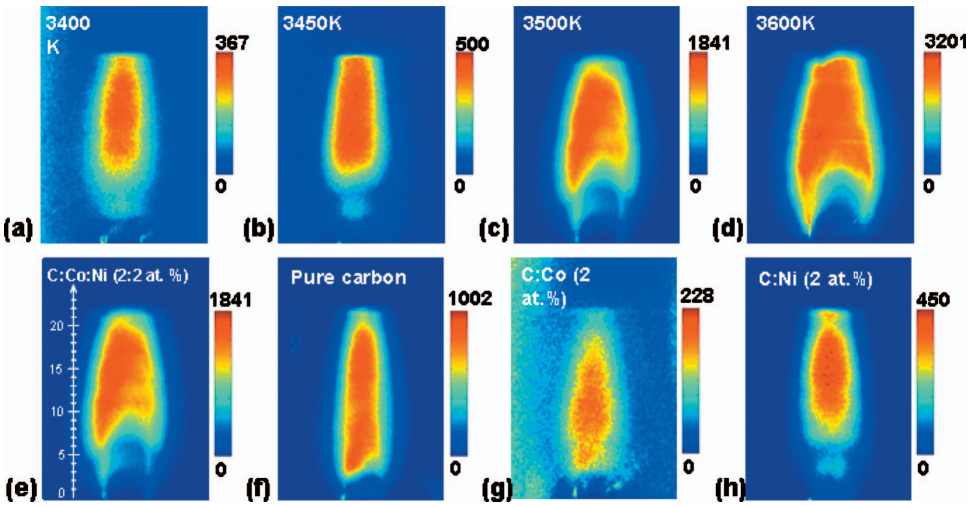

FIG. 17. (Color) Averaged soot LII images recorded in He (300 hPa, 50 ml s^{-1}): over C:Co:Ni target at (a) T_s=3400 K, (b) T_s =3450 K, (c) T_s=3500 K, and (d) T_s=3600 K. At T_s=3500 K over (e) C:Co:Ni, (f) pure carbon, (g) C:Co, and (h) C:Ni targets. Scale: number of counts on the CCD camera.

measurements. A single shot LII image gives an instantaneous view of the flow, which is laminar most of the time, but occasionally becomes turbulent, due to the surface irregularities. By relying on the temporal history of vaporization conditions (Fig. 2), a careful selection of the runs is performed prior to treatment and analysis of the data. The laminar regime is easily reproduced from run to run; and turbulent conditions, when they occasionally occur, are disregarded. Therefore, in the final set of runs, averaged image corresponds to a quantitative visualization of soot particles distribution since transient instabilities of the plume are smoothed over several tens of seconds.

Figures 17(a)–17(d) show first that the surface temperature of a C:Co:Ni target has a marked effect on the concentration of soot produced in the hot flow. The relative soot concentration is seen to increase by about a factor of 10 from 3400 to 3600 K. This result is in agreement with the rise of the vaporization rate from 0.3 to 3 mg s^{-1} in this temperature range, as measured in Fig. 2(b). Quantitative LII imaging is thus consistent with the previous weighting procedure.[14,22]

Second, the presence of Ni and Co catalysts in the target has a marked effect on the map of soot as shown in Figs. 17(e)–17(h). In the case of pure carbon target [Fig. 17(f)], a strong LII signal is observed close to the target surface whereas a top-hat shadow is observed in this area above C:Co:Ni and C:Ni targets [Figs. 17(e) and 17(h)]. This dark zone extends over 6 mm above the target, that is, up to the end of the thermal region 2. This phenomenon is even more obvious by considering the vertical soot distribution in Fig. 18. These 1D profiles have been extracted from the images along the flow center line, by taking an average over 10 pixels corresponding to about 640 μm, and providing the same spatial resolution as in LIF experiments (in Sec. III). We see clearly that these profiles strongly depend on the target composition. The signal first increases slowly up to h=3 mm and then stops increasing with a first maximum at h=4 mm and a slight decrease at h=5 mm. It thus exhibits a so-called "plateau," extending from 3.5 to 6 mm in height, that is in the region 2 of the temperature gradient (Fig. 3). The plateau only appears for the Ni-containing targets [Fig. 18(b)] whereas pure carbon target exhibits a regular behavior similar to C:Co target. The curve inflection observed for Ni-containing targets is located at h=3.5 mm in the middle of the shadow zone observed in the images. The LII signal is small in the shadow mainly because the sizes of the metal-carbon soot remain smaller than 4 nm, as measured in Fig. 16. It reveals that very small carbon aggregates are maintained (or stops growing) when height is ranging between 3.5 and 6 mm with the Ni-containing targets [Fig. 18(a)]. The amplitude of the LII signals reaches a second maximum beyond h=8 mm, which is two times stronger with Ni-Co catalysts than with pure carbon. A steep increase in signal amplitude is seen between 5.5 and 8 mm because the size of the soot is increasing very fast over the C:Co:Ni (96:2:2 at. %) targets (Fig. 16). That transformation is located just at the top of the dark zone observed on the images. The spatial location of this steep increase also corresponds to the end of region 2 (h=5.5 mm and $T\sim$1600 K) in the sketch of Fig. 3. This behavior can be fully understood from a cross correlation with LIF profiles as shown now.

First both the shadow effect in LII images and plateau in soot profiles, arising in region of the temperature gradient, can be well understood by correlating them to the plateau of the metal vapors observed in LIF in the same temperature region [Fig. 18(c)]. According to the LIF measurements, this thermal region 2 has been defined as the region where metal vapor transforms into metal particles. This correlation strongly suggests that the metal condensation has a drastic effect on the soot particle formation. It modifies the carbon aggregation and acts to change the soot size and density, yielding a very weak LII signal in the region 1. As shown in Fig. 16, carbon particles remain small (up to 5 mm) in the flow inside the region 2 where the plateau is observed in the soot profile. This means that in region 2, carbon clusters stop to aggregate, we propose to explain the inhibition of the

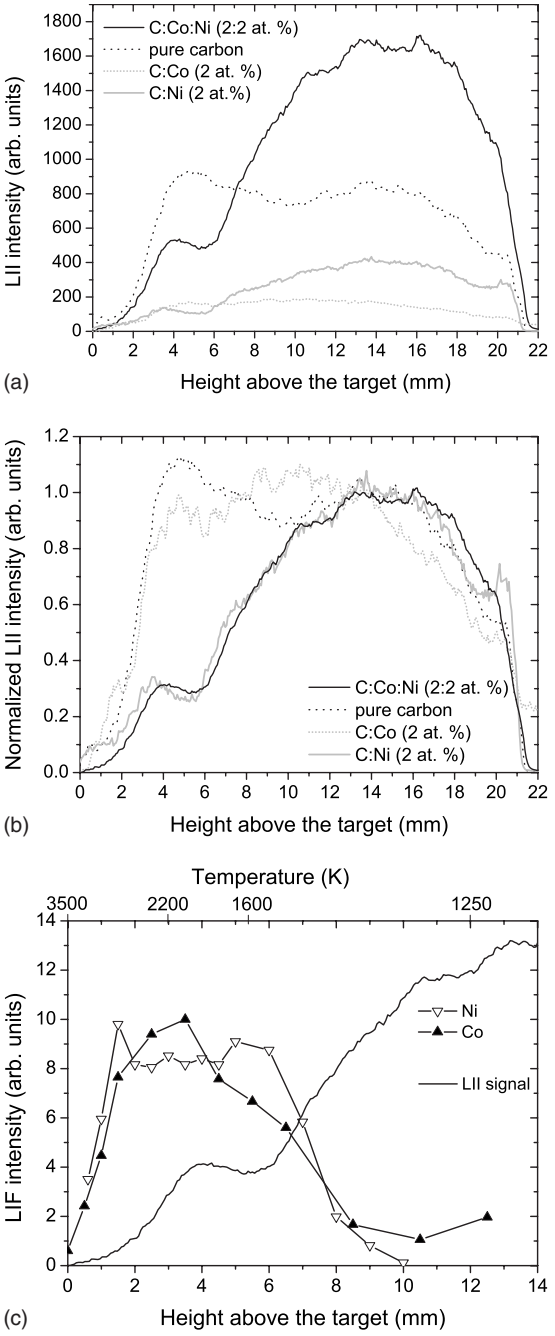

FIG. 18. (a) Center-line profiles of soot LII signal at T_s =3500 K in He (300 hPa, 50 ml s^{-1}) over C:Co:Ni, C:Co, C:Ni, and pure carbon targets. (b) The same profiles as (a) with intensity normalized at 14 mm.(c) Comparison between the profiles of Ni, Co LIF signals and the profile of soot LII signal over C:Co:Ni target. The temperatures between the different thermal regions as defined in Fig. 3 are given at top.

carbon aggregation by a dissolution of carbon clusters formed in region 1 into the metal particles growing in region 2.

Furthermore, comparison between the profiles obtained from the different target compositions indicates that the modification in the carbon aggregation seems to only occur for Ni-containing targets. In the case of carbon with only cobalt, the LII signal intensity is much weaker, with a spatial

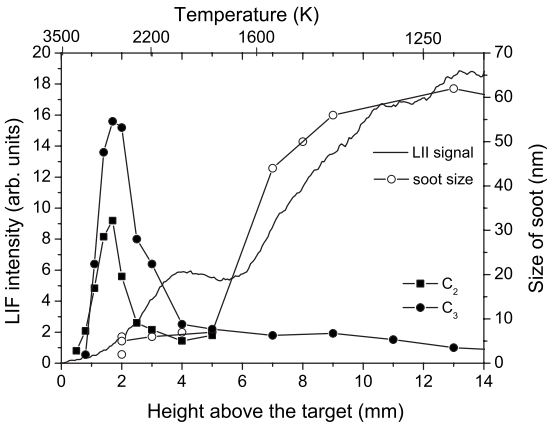

FIG. 19. Comparison between the profiles of C_2, C_3 LIF signals and the profile of soot LII signal over C:Co:Ni target at T_s =3500 K. The temperatures between the different thermal regions as defined in Fig. 3 are given at top.

distribution similar to the one observed on pure carbon targets [Fig. 18(a)]. This indicates that nickel only inhibits the aggregation of the carbon soot particles.

The LII signal is small in the shadow region mainly because the sizes of the metal-carbon soot remain smaller than 4 nm, as measured in Fig. 16. The shadow thus reveals the formation of nickel-carbon clusters that are probably molten since the temperature is greater than 2100 K below h =3.5 mm (Fig. 3). Step (a) of carbon dissolution in liquid metal particles occurs in this region as proposed in V-L-S model.[7–9] Moreover, the smallest LII intensity is observed with only cobalt in the target, probably due to a smaller overall size of the soot, with a diameter mainly under the detection threshold of LII (about 2 nm). Unfortunately, soot sizing was not possible over the C:Co targets because of the weakness of the LII signal.

Let us now correlate LIF profiles of C_2 and C_3 with the LII signals present in region 1 of the temperature gradient (Fig. 19). The region of the fast C_2 and C_3 depletion (2–2.5 mm) coincides with a slow increase in the LII signal due to primary soot particles formation and corresponds also to the onset of the plateau of metal catalyst vapors [Fig. 18(c)] in region 1 of the thermal gradient. If the first small carbon clusters are formed in this region, they may be the precursors of the primary active soot (Fig. 19). These active soot particles also interact with the nascent molten metal clusters soon after, beyond 3.5 mm in region 2 of the thermal gradient [Fig. 18(c)]. Moreover the LII signal is twice larger over the pure carbon target at h=4 mm [Fig. 18(a)] whereas the LIF signal of carbon radicals was twice smaller on that target [Figs. 5(a) and 8(a)]. It indicates that the carbon radicals concentration is smaller if the soot concentration is larger and the reverse. That observation of carbon transformation, although quite complex, is in good agreement with a carbon mass conservation all along the flow. Because of the much greater bond energy of carbon compared with Ni and Co, kinetics calculations have shown that carbon condenses much faster and at higher temperatures than Ni and Co. Ni and Co may interact with carbon to form clusters.[20] Let us recall that we have discriminate the Co and Ni behavior ob-

served by LIF (Sec. III B 2), thanks to the comparison with kinetics calculations.[21]

As shown in Figs. 18(a) and 16, soot profile intensity and carbon particle size both suddenly increase beyond $h=8$ mm, for metal-containing targets whereas for pure carbon target carbon soot further monotonously increases in size. This sudden increase occurs at the beginning of region 3 of the temperature gradient. In particular, in C:Co:Ni targets, carbon particle size increases up to 60 nm whereas it remains below 30 nm for pure carbon target. The drastic increase in presence of metals evidences the onset of a new kind of carbon structures, which have typical sizes much larger that those found in pure carbon soot. Knowing the huge form aspect of the nanotubes, this strongly suggests to correlate the discontinuity observed in the LII signals to the nanotube onset and to describe it as proceeding by a carbon segregation from the metallic phase. The present experiment is an evidence of the *in situ* observation of carbon nanotubes in high-temperature processes.

VI. SPECIAL BEHAVIOR OF Fe AS TARGET IMPURITY

Iron was found to be present as an impurity in the targets used in our experiments. Both LIF and LII were applied on C:Fe (98:2 at. %) targets and on carbon targets containing Fe impurities to study the particular behavior of Fe. Thanks to its strong fluorescence efficiency, it can be detected very easily. Measurements have revealed that, because of its low concentration in the system, Fe behaves differently than Ni and Co in soot profiles.

Figure 20(a) presents a typical dispersed fluorescence spectrum of iron atom obtained above a carbon target containing iron impurities. The laser frequency is set to the top of line 6 observed in the excitation spectrum [Fig. 20(b)] and assigned in Table III. The strongest fluorescence bands are located at 248 nm (resonant band) and 300 nm (nonresonant band). The transitions of iron atoms are much stronger than those of nickel and cobalt atoms within that spectral window (by more than a factor of 100, Table III). Therefore, the LIF signal originating from trace amounts of iron is readily detected. A molar fraction of about 0.09% is calculated at 3 mm and $T_s=3500$ K from the ratio of LIF signals measured on a carbon target and on a C:Fe (98:2 at. %) target by assuming that the signal is linear in concentration.

In Fig. 21 both LIF and LII results are cross correlated. In Fig. 21(a), the LIF signals of iron [line 4 in Fig. 20(b) and Table III] are plotted vs height above carbon and C:Fe targets at $T_s=3500$ K. In the latter plot, a careful check is done to prevent saturation of the detector. The Fe signal is strong enough, even for trace amount of iron, to saturate the detector at $T_s=3500$ K. Thanks to the huge LIF signal induced on line 4, the tiny population of Fe atoms lying in their ground electronic state is large enough to be probed inside the vaporization layer. The LIF signals of Ni and Co have not been detected in this zone where all species are assumed to be highly excited (Figs. 10 and 11). Therefore this measurement is the only one detecting the metal vapor lying inside the first millimeter over the target surface. A peak of signal is clearly seen at $h=0.5$ mm in Fig. 21(a) thus showing that solid

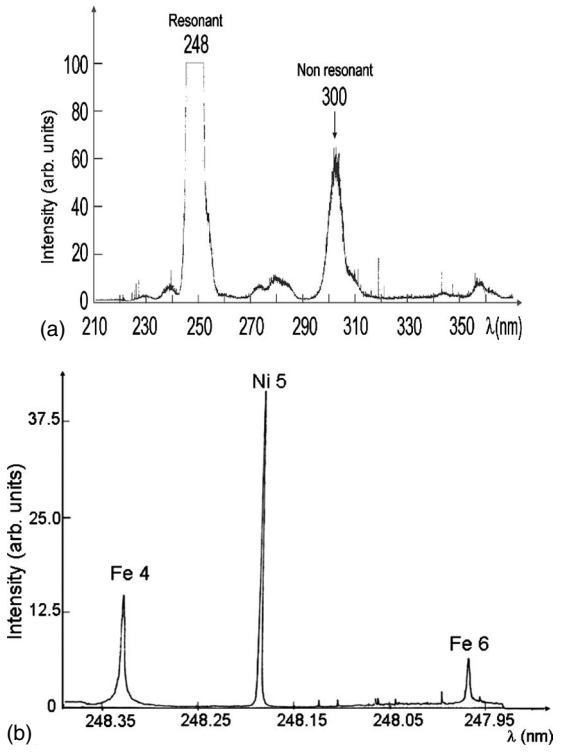

FIG. 20. (a) Dispersed fluorescence spectrum (resolution of 4 nm) with the laser tuned to line 6 of Fe (Table III) recorded at 4 mm above a pure carbon target at $T_s=3200$ K in He (300 hPa, 50 ml s^{-1}). (b) Excitation spectrum recorded at 6.5 mm above a C:Co:Ni (2:2 at. %) target at $T_s=3200$ K with detection set at 300 nm (bandwith=4 nm). Three lines are observed: lines 4 and 6 of Fe as impurity and line 5 of Ni 2 at. % (see Table III for spectroscopic data).

angle of the detection channel is not limiting optical probing of the vaporization layer. The LIF signal of Fe then rapidly decreases due to fast cooling and metal clusters formation. It is reasonable to assume that atomic metal vapor is predominantly formed just above the target surface and then suddenly drops to a lower level in good agreement with the kinetics calculations of metal clusters formation and growth.[3,20,21] This metal atom behavior observed in the first millimeter region corresponds to recombination of Fe atoms to form dimers and then agglomeration into small clusters which may also be predicted from its Fe-Fe bond energy as for Ni and Co.[21] A first minimum is observed at 2 mm on the LIF profile recorded at 3500 K; thus corresponding to the end of the vaporization layer. Soon above 2 mm, iron vapor concentration increases again to reach another plateau which seems to continuously increase; the plateau is spreading up to the onset of the tube. The rates of evaporation and cluster growth are driving the appearance and stretch of the Fe vapor phase.

In the case of C:Fe (2 at. %) target, the signal increases beyond 2 mm to form a large plateau behavior. As for Ni and Co, this profile indicates the transformation of metal cluster inside region 2 of the temperature gradient; but with a different reactivity.[50] Over the C:Fe target, the plateau ends between 10 and 12 mm because of dilution (2% metal in helium carbon), but also because of the lower melting tem-

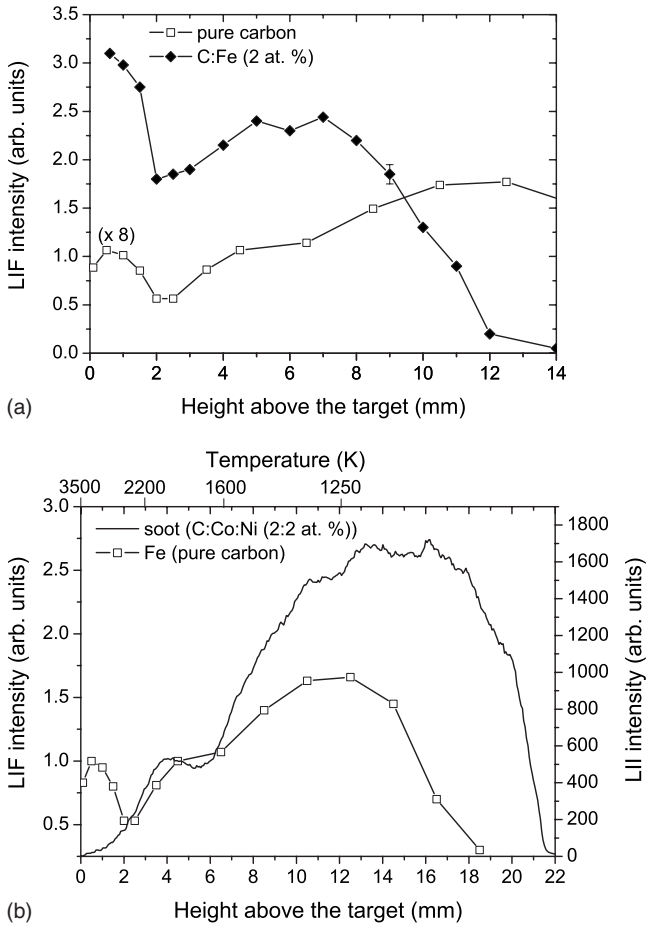

FIG. 21. (a) Spatial evolution of LIF signal of Fe (line 4) for C:Fe and pure carbon targets at T_s=3500 K in He (300 hPa, 50 ml s^{-1}). For the sake of clarity, the signal intensity is multiplied by 8 in the case of pure carbon. (b) Comparison between the evolution of LIF signal of Fe for a carbon target and the evolution of LII signal of soot particles for C:Co:Ni target.

perature of iron (1400 K) compared to nickel and cobalt (1600 K). When the gas temperature decreases below 1200 K at 12 mm, it is reasonable to assume that iron particles are fully condensed. However, iron has a very peculiar behavior over the pure carbon target. In such a low molar fraction (0.1%), iron atoms are seen to persist in the carbon flow up to 18 mm [Fig. 21(a)] but the signal slowly decreases between 14 and 18 mm. when the metal is highly diluted in the carbon-helium flow, and since dilution is known to drive the spatial extent of the plateau, its vapor extends toward much lower temperature. We can assume that size effect also contributes to the longer persistence of Fe atoms by influencing the phase transformation of the metal-carbon nanoparticle.[51] We see that equilibrium is maintained between the Fe gas and the forming clusters mainly composed of carbon so that Fe gas signal is observed far above the target, namely, up to a region where the temperature is lower than the melting temperature of the Fe-C system. This observation is reasonable since melting temperature decreases as the particle size decreases. The TEM images show that the size of metal particles is around 7 nm [Fig. 13(c)]. For such a nanoparticle size, the melting temperature of Fe-C can be as low as about 1000 K.[52]

In Fig. 21(b), the LIF profile of iron is compared to the LII profile to allow direct comparison between signals from gaseous (iron) and solid phases (soot). A curve inflection is observed between 4 and 6 mm on the two profiles suggesting that metal modifies the carbon aggregation at that stage (size <4 nm). The correspondence of the metal and soot plateau between 2.5 and 6.5 mm is quite important because it brings an additional proof of metal-carbon interaction at the primary stage of cluster formation in region 2 of the thermal gradient. However, in the region 3, the signal of iron is still similar to that of soot. Therefore, because iron is below 0.1 at. % in carbon targets, it definitely does not act as a catalyst, but simply flows along with the carbon clusters. In summary, the concentration of catalysts is seen to act on the cluster composition and size. It has a dominant influence on the phase transformation and on the condensation temperature of the metal-carbon aggregates. When its concentration is high enough (>1 at. %), it may start to act as a catalyst.

In C:Fe samples, large particles, surrounded by smaller particles, are seen in TEM images [Fig. 13(c)]. It is known that an over saturation of carbon in iron (25 at. %) can generate the iron carbide Fe_3C (cementite) (Table I), which may be formed at the surface of each iron particle.[51] Isolated pure metal particles of small sizes are also present. Our attempt to assign the coverage of each particle by Fe_3C carbide is supported by the observations of Gavillet *et al.* in the case of Ni-Y catalyst mixtures. In that latter case, high-resolution TEM images have shown that Ni particles are covered by platelets of stable YC_2 carbide.[8,12] The formation of the yttrium carbide at the particle surface is favored by two properties of yttrium: its ability to form a stable carbide in solid state at a medium temperature ($T_{\text{formation}}$=2563 K, Table I), and its low surface energy compared to that of Ni.[12] Conversely, Ni and Co do not form stable carbides.[5,21] Since Fe_3C carbide is formed at 1525 K, it is likely formed in region 3 of the thermal gradient [Fig. 3(b)]. At that location carbon migrates to form the nanotube nuclei at the surface of the particle as predicted in nucleation step of the V-L-S model.[8,9] Since diffusion of carbon through Fe_3C is slower than through pure iron particle,[51] tube growth is probably blocked. Therefore Fe catalyst, when used alone, is less effective than Ni or Co to produce SWCNTs in our synthesis conditions, owing to its carbide formation. As a matter of fact, no nanotube is formed in the C:Fe samples whereas the C:Ni and C:Co samples contain a few nanotubes. This finding is consistent with the SWCNTs yield following the order $C:Co:Ni > C:Ni \gg C:Co \sim C:Fe$, observed in pulsed laser ablation process by Yudasaka *et al.*,[43] who showed that the yield of SWCNTs in CO_2-laser vaporization and in arc discharge processes give a similar order of catalyst efficiencies.

VII. DISCUSSION

In this paper, laser-based diagnostic techniques are used to investigate the chemistry of the hot carbonaceous flow including catalyst nanoparticles. The main results of optical measurements of catalyst atoms, C_2, C_3 radicals and soot

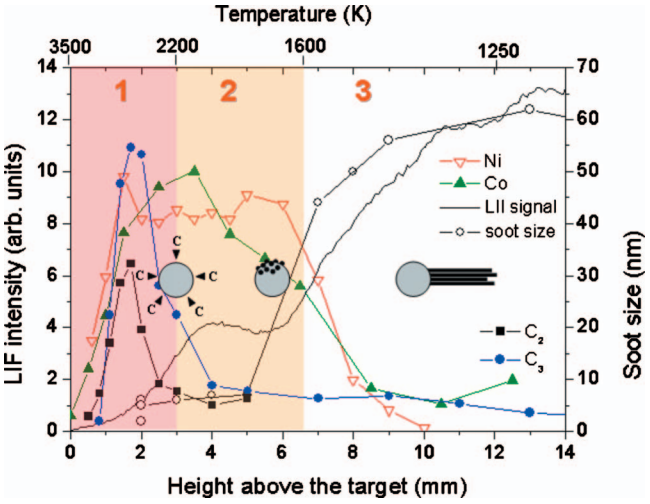

FIG. 22. (Color) Summary of the *in situ* optical diagnostics of Ni, Co, Fe, C_2, C_3, and soot particles (size and LII signal) obtained over C:Co:Ni targets. The thermal regions as defined in Fig. 3 and the scenario of nanotube formation as proposed by Gavillet *et al.* (Ref. 8) are reported.

particles together with the predicted concept of nanotube growth drawn from the V-L-S model[7–9] are summarized in Fig. 22.

Just above the target, the vaporized carbon and metal species are produced and then rapidly start to aggregate in the hot flow. The region of metallic vapor transformation is located by comparing the behavior of different target compositions using LII. Carbon condensation is observed using LIF of carbon radicals and LII of condensed carbon particles (soot). The size evolution of the soot is drawn from the time-resolved LII signals and the main region of soot particle growth are thus identified. The long quasi-isothermal zone (T=1500–1000 K) is equivalent to a natural oven in favor of SWCNTs growth (Fig. 3). Starting from the temperature profile, several zones have been defined in which carbon molecules and metallic atoms are probed.

Our observations have first demonstrated that the primary condensation of carbon takes place in the 2–3 mm region, that is, in region 1 of temperature gradient (Fig. 22). At the end of this region, the C_2 signal vanishes indicating that most carbon atoms of the vapor phase are already recombining. Therefore region 1 can be defined as the region where the primary condensation of carbon takes place. Furthermore, within the vaporization layer (1–2 mm above the target), the C_2 radical is found to be mainly formed in electronic and vibrational excited states. It is shown that the depletion of the C_2 signal is accelerated by Co catalyst indicating the existence of strong interactions between the radical and this metal leading to the possible formation of CoC_2 radicals or small Co-C clusters. A main difference between the Ni and Co catalyst is thus evidenced here in the gas phase by the C_2 behavior. The present results are evidence of a different behavior of Ni and Co and a different reactivity with C.

Ni and Co profiles (Figs. 10 and 11) have shown that the signal levels off between 2 and 6 mm and finally vanishes at about 8 mm, that is at the end of region 2 of the temperature gradient (Fig. 22). The vanishing of the LIF signal means that metal atoms have disappeared from the gas phase and are fully condensed into liquid or solid clusters and particles. Therefore the region 2 of the temperature gradient can be defined as the region where the metal gas transforms into a condensed (liquid and solid) phase.

The evolution of the catalyst vapor is calculated in Ref. 21 but some of them require a deeper interpretation and comparison with other results presented here. In the chemical kinetic model, the evolution of metal atoms is mainly driven by the condensation/evaporation routes of metal clusters interacting with carbon at different stages of the synthesis.[20] The concentration of Ni and Co atoms in the gas phase results from the condensation/evaporation rates of Ni and Co clusters, which are based on the bond energy of the Ni-Ni and Co-Co dimers. The calculations of Ni and Co atoms evolutions well reproduce the experimental LIF profiles, demonstrating that the plateau is due to the existence of a metal vapor around liquid growing particles in supersaturation conditions. This gas dynamics, by contrast to static calculation, is found to play a major role and to result from the cooling conditions.

Nickel condensation appears later in the plume and the calculation of the condensation/evaporation process has evidenced the effect of metal dilution.[21] By contrast with Ni, Co signal decreases sooner and the particular behavior of Co atoms, is attributed to a faster agglomeration into Co-C clusters, caused by an early interaction between Co and C in the gas phase, as revealed by LIF measurements. Here, an additional evidence that a particular interaction takes place with Co is given which can be reasonably associated with the ability of Co to promote the segregation of carbon at the surface of metal-carbon clusters.

The shadow effect observed in the LII images and the plateau in soot profiles (solid line) and arising in the region 2 of temperature, can be well understood by correlating them to LIF plateau of Ni and Co observed concomitantly. This correlation strongly suggests that the metal condensation, responsible for the LIF plateau, has a drastic effect on the soot particle formation. It modifies the carbon aggregation and acts to change the soot size and density, yielding a very weak LII signal in the region 2. This means that in region 2, carbon clusters stop to aggregate. We propose to explain the inhibition of the carbon aggregation by a dissolution of carbon clusters formed in region 1 into the nickel particles growing in the region 2. Such a dissolution is quite still possible owing to the carbon solubility ability of metal liquid phases according to Co (Ni)-C phase diagrams.

In Fig. 22, soot profile intensity and carbon particle size both suddenly increase beyond h=8 mm, for metal-containing targets whereas for pure carbon target, carbon soot monotonously increases in size [Fig. 16(b)]. This sudden increase occurs at the beginning of region 3 of the temperature gradient. In particular, in Ni-containing targets, carbon particle size increases up to 60 nm whereas it remains below 30 nm for pure carbon target. The drastic increase in presence of metals evidences the onset of a new kind of carbon structures, which have typical sizes much larger that those found in pure carbon soot. Knowing the huge form aspect of the nanotubes, this strongly suggests to correlate the discontinuity observed in the LII signals to the nanotube

onset and to describe it as proceeding by a carbon segregation from the metallic condensed phase. The present experiment is an evidence of the *in situ* observation of carbon nanotubes.

All our results provide an experimental proof of the processes involved in the V-L-S model describing the nucleation and growth of SWCNTs. They completely confirm that, as assumed in this model, tube nucleation proceeds via a dissolution of C into metal droplets followed by its segregation when C gets supersaturated. Beyond this qualitative confirmation, experimental results provide new quantitative information and a deeper knowledge of the role played by the metal catalysts.

First, cross linking of LIF and LII data (Fig. 22) let us establish that nanotube onset occurs at a gas temperature equal to about 1700 K, that is at a temperature close the eutectic plateau of Ni(Co)-C system. This confirms that the nanotube nucleation driving force is the solubility difference of carbon between metallic solid and liquid phases. Second, we can discriminate, from our results, the roles played by the different metal catalysts in this dissolution-segregation process. In contrast to Co, Ni is found to be able to dissolve a large amount of carbon, and also to condense at a slower rate.[21] This different behavior results from the difference in the reactivity with C in the gas phase which is responsible for the formation of small Co-C and large Ni-C clusters. The histograms of the sizes of nanoparticles, which are measured from the TEM images of our synthesized samples, support that assertion (Fig. 14). Indeed, *ex situ* TEM measurements show that the average Co particle size is small (5.5–8.5 nm), with a narrow distribution of size (at most 18 nm), while Ni particles exhibit a broader distribution of size (at most 70 nm). Furthermore, LII signal recorded over C-Co targets are very weak and the soot size measurement was not possible in that case. The weakness of the signal also reveals that soot particles are too small to produce efficient incandescence signal with only cobalt in the target. Therefore, *ex situ* and *in situ* results indicate that segregation is faster with cobalt (small Co-C particles) and dissolution of carbon is faster with nickel (larger Ni-C particles).

Finally, Fe is shown to display a peculiar behavior. Iron atoms are seen to persist much longer in the gas plume than Ni and Co atoms, where the concentration plateau covers regions 1–3 of the plume (Fig. 22). Persistence partly results from the melting temperature of Fe-C, which is almost 200 K lower than the melting temperatures of Ni-C and Co-C (Table I). Furthermore, it is well known that the melting temperature of a metal carbide is heavily dependent on the size of the nanoparticles.[11,52,53] Louchev *et al.*[52] have calculated the melting temperature as a function of nanoparticle size. For a nanoparticle of 10 nm in diameter, Fe-C melts at 1035 K, Co-C at 1180 K, and Ni-C at 1200 K. However, for 60 nm nanoparticles, Fe-C melts below 1300 K (see Fig. 9 in Ref. 52). The decrease in the melt temperature with the particle size decrease is confirmed by the molecular-dynamics calculations done by Ding *et al.*[11,53] These calculations show that both coalescence and melting temperatures of iron clusters decrease linearly with decreasing cluster size. For instance, 1 nm particles melt below 800 K, whereas particles larger than 3 nm are solid around 1200 K.[11] In that context, it is reasonable to assume that the LIF signal originates from the gas surrounding very small Fe particles which stay molten nearly up to region 3 while Ni-C and Co-C carbon particles are already solid in region 3. We recall that iron has the propensity to form a stable carbide Fe_3C at 1500 K (Sec. VI). Since iron is in trace amounts in carbon targets ($<0.1\%$), the dilution is large in helium and the plateau extends up to $h=15$ mm (Fig. 21), where large soot particles are also seen (Fig. 22). That particular behavior of the iron LIF signal is explained by the fact that with such high dilution in gas, iron atoms cannot condense as rapidly and therefore cannot play the role of an active catalyst. Furthermore, kinetics calculations of the evolution of Ni and Co have shown that the plateau of metal atoms is significantly extended by increasing the dilution of metal in the gas flow. The exceptionally high detectivity of iron by LIF has opened a new possibility of monitoring both the condensed (soot) and gaseous (iron atoms) species in the vaporized plume [Fig. 21(b)].

VIII. SUMMARY

This study combined *in situ* LII and LIF investigations of the metal-carbon catalysts in the vaporized plume of SWCNTs production by cw CO_2-laser vaporization. The study has made possible the identification of the different steps of condensation of primary carbon and metal gas phases issued from the vaporization of the target and their association with the V-L-S model of SWCNTs growth. We have been able by combining temperature, carbon soot, and metal gases measurements, using different spectroscopic techniques (CARS, LIF, and LII), to identify all the steps involved in the V-L-S model. Beyond this qualitative confirmation of the validity of this model, we have been able to determine at which temperatures, the different steps occur leading to a deeper knowledge on the role played by the metal on the condensation process of the carbon soot. One of the key results is the evidence that metal has a crucial impact at different steps of carbon condensation, depending on its chemical nature.

The nucleation and growth mechanism emerging from the present study can be summarized as the following. Both metal and carbon are vaporized in highly excited electronic and vibrational states, which are relaxing within a layer of 1mm in height above the target surface. Condensation of these vapor phases is driven by the temperature gradient lying in the reactor. Three temperature regions can be defined, as they are related to different condensation and phase transformation processes. Carbon is observed to condense first, both by LII and LIF. The temperature region 1 is defined as the region where the primary condensation takes place, as attesting by the vanishing of C_2 and C_3 LIF signals and the onset of soot particle growth as evidenced by LII measurements of particle sizes. It is ranging from 3500 to 2200 K, is characterized by the highest cooling rate, and extends up to 3 mm above the target surface. At the end of region 1, size of carbon aggregates is below 5 nm, according to LII measurements. One key result of our study is the evidence that, even in this step, carbon aggregation is perturbed by the presence of the metal gas phase. Co atoms of the gas phase are found

to strongly interact with the C_2 radical to form Co-C clusters. Such a behavior is not observed for Ni, and Ni and Co impact differently carbon condensation. In opposition to C_2, the evolution of C_3 is not affected by the presence of cobalt catalyst in the gas phase, indicating that the carbon trimer only contributes to soot growth.

Below 2200 K carbon condensation is even more perturbed by the presence of metals. Ni is now specifically responsible for this perturbation and this is the second difference between Ni and Co. When C is vaporized alone or together with Co, C aggregates gently grow in size, following a linear evolution as a function of temperature, as attested by LII measurements. In presence of Ni, soot growth is stopped until 1600 K, which gives rise to a shadow region of the hot carbonaceous plume observed in LII images. This temperature region ranging from 2200 K up to 1600 K is defined as the region 2 and is identified as the region where metal gas phases are condensing into liquid particles. There is no *in situ* technique able to follow directly the formation and the growth of these particles. However, metal condensation could be identified thanks to the study of metal gas phases by LIF. LIF signal is indeed found to remain constant in region 2 and to abruptly vanishes at 1600 K. The occurrence of this plateau is shown to be due to a metal vapor necessarily in a condition of high supersaturation around condensing particles. The sudden drop of metal atom vapor is explained by the condensation of the metal vapor which can take place at that location because the temperature decreases below the melting temperature. It is obvious that the vapor pressure has an abrupt change as the condensed phase changes from liquid to solid. The concomitance between Ni condensation and the inhibition of carbon soot growth means that the first phenomenon has a dramatic effect on the latter, which can only be explained by the dissolution of C clusters into growing Ni particles. This effect is not observed for Co because Co is reacting with C much earlier in the gas phase to directly form Co-C clusters. These different reaction processes attest the difference in the size distribution of Co and Ni particles measured *ex situ* on TEM images.

The region 3, starting below 1600 K is finally identified as the region of nucleation and growth of carbon nanotubes. Nanotubes onset is evidenced by the sudden rise in the LII signal occurring in this region, which is not observed in absence of metal, but which results from an abrupt segregation effect between C and Ni. Carbon dissolved in these particles is suddenly released, giving rise to a new kind of carbon structures with characteristic sizes which are not observed when no metal is vaporized along with carbon. The only possible structures are carbon nanotubes.

In conclusion, the inhibition of the carbon soot growth in region 2 followed by the sudden growth of a large size structure in region 3 is the experimental evidence of the carbon dissolution/segregation process from metal particles underlying the nanotube nucleation. Ni is found to be mainly responsible for this process. Our study shows that Ni and Co play in fact complementary roles. On one hand, Co accelerates the primary aggregation of C and the formation of Co-C clusters in the gas phase, thus contributing to impede the formation of large C aggregates. On the other hand, Ni favors dissolution of C while condensed in liquid particles, which is essential to create a high segregation driving force for nanotube nucleation upon solidification of the particles. This complementary role explains why better yields are obtained when using a bimetallic Ni-Co catalyst rather than pure Ni or pure Co.[5]

ACKNOWLEDGMENTS

This work has been done in the framework of the GDRE No. 2756 "Science and application of the nanotubes-NANO-E." We are very grateful to F. Ducastelle and H. Amara for helpful discussions. We thank G. Désarmot for taking care of target production.

*nelly.dorval@onera.fr
†Present address: 492 Enchanted Oak, New Braunfels, TX 78132, USA.

[1] C. Journet, W. K. Maser, P. Bernier, A. Loiseau, M. L. de la Chapelle, S. Lefranc, P. Deniard, R. Lee, and J. E. Fischer, Nature (London) **388**, 756 (1997).
[2] C. Scott, S. Arepalli, P. Nikolaev, and R. Smalley, Appl. Phys. A **72**, 573 (2001).
[3] C. D. Scott, A. Povitsky, C. Dateo, T. Gökçen, P. A. Willis, and R. E. Smalley, J. Nanosci. Nanotechnol. **3**, 63 (2003).
[4] A. A. Puretzky, H. Schittenhelm, X. Fan, M. J. Lance, L. F. Allard, Jr., and D. B. Geohegan, Phys. Rev. B **65**, 245425 (2002).
[5] D. Laplaze, L. Alvarez, T. Guillard, J. M. Badie, and G. Flamant, Carbon **40**, 1621 (2002).
[6] E. Muñoz, W. K. Maser, A. M. Benito, M. T. Martinez, G. F. de la Fuente, A. Righi, J.-L. Sauvajol, E. Anglaret, and Y. Maniette, Appl. Phys. A **70**, 145 (2000).
[7] J. Gavillet, A. Loiseau, C. Journet, F. Willaime, F. Ducastelle, and J.-C. Charlier, Phys. Rev. Lett. **87**, 275504 (2001).
[8] J. Gavillet, A. Loiseau, F. Ducastelle, S. Thair, P. Bernier, O. Stephan, J. Thibault, and J.-C. Charlier, Carbon **40**, 1649 (2002).
[9] J. Gavillet, Ph.D. thesis, Université Paris VI, 2001.
[10] Y. Saito, Carbon **33**, 979 (1995).
[11] F. Ding, A. Rosen, and K. Bolton, J. Nanosci. Nanotechnol. **6**, 1211 (2006).
[12] J. Gavillet, J. Thibault, O. Stephan, H. Amara, A. Loiseau, C. Bichara, J.-P. Gaspard, and F. Ducastelle, J. Nanosci. Nanotechnol. **4**, 346 (2004).
[13] M. Castignolles, A. Foutel-Richard, A. Mavel, J. L. Cochon, D. Pigache, A. Loiseau, and P. Bernier, in *Structural and Electronic Properties of Molecular Nanostructures*, AIP Conference Proceedings Vol. 633, edited by H. Kuzmany, J. Fink, M. Mehring, and S. Roth (AIP, New York, 2002), p. 385.
[14] A. Foutel-Richard, Ph.D. thesis, CNAM-Paris, 2003.
[15] M. Castignolles, Ph.D. thesis, Université Montpellier II, 2004.
[16] A. A. Puretzky, D. B. Geohegan, X. Fan, and S. J. Pennycook,

Appl. Phys. A **70**, 153 (2000).
[17] S. Arepalli, P. Nikolaev, W. Holmes, and C. D. Scott, Appl. Phys. A **70**, 125 (2000).
[18] N. Dorval, A. Foutel-Richard, M. Cau, A. Loiseau, B. Attal-Trétout, D. P. J.-L. Cochon, P. Bouchardy, V. Krüger, and K. P. Geigle, J. Nanosci. Nanotechnol. **4**, 450 (2004).
[19] V. Krüger, C. Wahl, R. Hadef, K. P. Geigle, W. Stricker, and M. Aigner, Meas. Sci. Technol. **16**, 1477 (2005).
[20] C. D. Scott, J. Nanosci. Nanotechnol. **4**, 368 (2004).
[21] M. Cau, N. Dorval, B. Cao, B. Attal-Trétout, J.-L. Cochon, A. Loiseau, S. Farhat, and C. D. Scott, J. Nanosci. Nanotechnol. **6**, 1298 (2006).
[22] M. Cau, Ph.D. thesis, Université Paris XI, 2007.
[23] J. G. Phillips and S. P. Davis, *The Berkeley Analysis of Molecular Spectra* (University of California Press, Berkeley, 1968), Vol. 2.
[24] C. V. V. Prasad and P. F. Bernath, Astrophys. J. **426**, 812 (1994).
[25] A. Tanabashi and T. Amano, J. Mol. Spectrosc. **215**, 285 (2002).
[26] U. Rahmann, A. Bülter, U. Lenhard, R. Düsing, D. Markus, A. Brockhinke, and K. Kohse-Höinghaus, University of Bielefeld, Faculty of Chemistry, Physical Chemistry I, LASKIN- a simulation program for time-resolved LIF spectra, http://pc1.uni-bielefeld.de
[27] J. Luque, W. Juchmann, and J. B. Jeffries, J. Appl. Phys. **82**, 2072 (1997).
[28] G. P. Smith, C. Park, J. Schneiderman, and J. Luque, Combust. Flame **141**, 66 (2005).
[29] F. Kokai, K. Takahashi, and S. Iijima, J. Phys. Chem. B **103**, 8686 (1999).
[30] S. Arepalli, C. D. Scott, P. Nikolaev, and R. Smalley, Chem. Phys. Lett. **320**, 26 (2000).
[31] L. Gausset, G. Herzberg, A. Lagerqvist, and B. Rosen, Astrophys. J. **142**, 45 (1965).
[32] D. W. Tokaryk and D. E. Chomiak, J. Chem. Phys. **106**, 7600 (1997).
[33] I. Čermák, M. Föderer, I. Cermakova, S. Kalhofer, H. Stopka-Ebele, G. Monninger, and W. Krätschmer, J. Chem. Phys. **108**, 10129 (1998).
[34] J. P. Maier, N. Lakin, G. A. H. Walker, and D. A. Bohlender, Astrophys. J. **553**, 267 (2001).
[35] T. Oka, J. A. Thorburn, B. J. McCall, S. D. Friedman, L. M. Hobbs, P. Sonnentrucker, D. E. Welty, and D. G. York, Astrophys. J. **582**, 823 (2003).
[36] H. R. Leider, O. H. Krikorian, and D. A. Young, Carbon **11**, 555 (1973).
[37] G. De Boer, S. Arepalli, W. Holmes, P. Nikolaev, C. Range, and C. D. Scott, J. Appl. Phys. **89**, 5760 (2001).
[38] X. Fan, R. Buczko, A. A. Puretzky, D. B. Geohegan, J. Y. Howe, S. T. Pantelides, and S. J. Pennycook, Phys. Rev. Lett. **90**, 145501 (2003).
[39] E. Dujardin, C. Meny, P. Panissod, J. P. Kintzinger, N. Yao, and T. W. Ebbesen, Solid State Commun. **114**, 543 (2000).
[40] A. N. Andriotis, M. Menon, and G. Froudakis, Phys. Rev. Lett. **85**, 3193 (2000).
[41] X. Z. Liao, A. Serquis, Q. X. Jia, D. E. Peterson, Y. T. Zhu, and H. F. Xu, Appl. Phys. Lett. **82**, 2694 (2003).
[42] C. Rey, M. M. G. Alemany, O. Dieguez, and L. J. Gallego, Phys. Rev. B **62**, 12640 (2000).
[43] M. Yudasaka, Y. Kasuya, F. Kokai, K. Takahashi, M. Takizawa, S. Bandow, and S. Ijima, Appl. Phys. A **74**, 377 (2002).
[44] L. A. Melton, Appl. Opt. **23**, 2201 (1984).
[45] H. A. Michelsen, P. O. Witze, D. Kayes, and S. Hochgreb, Appl. Opt. **42**, 5577 (2003).
[46] M. Tsurikov, K. Geigle, V. Krüger, Y. Schneider-Kuhme, W. Stricker, R. Luckerath, R. Hadef, and M. Aigner, Combust. Sci. Technol. **177**, 1835 (2005).
[47] X. Mercier, A. Therssen, P. Desgroux, and J. F. Pauwels, Chem. Phys. Lett. **299**, 75 (1999).
[48] T. Ni, J. A. Pinson, S. Gupta, and R. S. Santoro, Appl. Opt. **34**, 7083 (1995).
[49] S. Farhat and C. D. Scott, J. Nanosci. Nanotechnol. **6**, 1189 (2006).
[50] H. Kanzow, C. Lenski, and A. Ding, Phys. Rev. B **63**, 125402 (2001).
[51] C. Klinke, J. M. Bonard, and K. Kern, Phys. Rev. B **71**, 035403 (2005).
[52] O. L. Louchev, H. Kanda, A. Rosen, and K. Bolton, J. Chem. Phys. **121**, 446 (2004).
[53] F. Ding, A. Rosen, and K. Bolton, Phys. Rev. B **70**, 075416 (2004).